

# Impact of Highest Maximum Sustained Wind Speed and Its Duration on Storm Surges and Hydrodynamics Along Krishna-Godavari Coast

Maneesha Sebastian (✉ [maneeshasebastian@gmail.com](mailto:maneeshasebastian@gmail.com))

Indian Institute of Technology Bombay <https://orcid.org/0000-0002-6602-4473>

Manasa Ranjan Behera

Indian Institute of Technology Bombay

---

## Research Article

**Keywords:** Tropical Cyclone, Rapid intensification, Gradual intensification, Duration of Intensification, Storm Surge, Hydrodynamics

**Posted Date:** May 10th, 2021

**DOI:** <https://doi.org/10.21203/rs.3.rs-241625/v1>

**License:**   This work is licensed under a Creative Commons Attribution 4.0 International License.

[Read Full License](#)

---

**Version of Record:** A version of this preprint was published at Climate Dynamics on February 19th, 2022. See the published version at <https://doi.org/10.1007/s00382-022-06173-9>.

1 **Impact of highest maximum sustained wind speed and its duration on storm surges and**  
2 **hydrodynamics along Krishna-Godavari coast**

3 Maneesha Sebastian<sup>1,\*</sup>, Manasa Ranjan Behera<sup>1,2</sup>

4 <sup>1</sup>Department of Civil Engineering, Indian Institute of Technology Bombay, Mumbai,  
5 Maharashtra 400076, India,

6 <sup>2</sup>Interdisciplinary Program in Climate Studies, Indian Institute of Technology Bombay,  
7 Mumbai 400076, India,

8

9 \*Corresponding author:

10 Dr. Maneesha Sebastian

11 Department of Civil Engineering,

12 Indian Institute of Technology Bombay,

13 Powai, Mumbai – 400076, India.

14 Email id: maneeshasebastian@gmail.com

15 orcid: <https://orcid.org/0000-0002-6602-4473>

16

17

18

19

20

21

22

## 23 ***Abstract***

24 The storm surge and hydrodynamics along the Krishna-Godavari (K-G) basin are examined  
25 based on numerical experiments designed from assessing the landfalling cyclones in Bay of  
26 Bengal (BoB) over the past 38 years with respect to its highest maximum sustained wind speed  
27 and its duration. The model is validated with the observed water levels at the tide gauge stations  
28 at Visakhapatnam during *Helen (2013)* and *Hudhud (2014)*. Effect of gradual and rapid  
29 intensification of cyclones on the peak water levels and depth average currents are examined  
30 and the vulnerable locations are identified. The duration of intensification of a rapidly  
31 intensifying cyclone over the continental shelf contributed to about 10-18 % increase in the  
32 peak water levels, whereas for the gradually intensifying cyclone the effect is trivial. The  
33 inclusion of the wave-setup increased the peak water levels up to 39% compared to those  
34 without wave-setup. In the deep water region, only rapidly intensifying cyclones affected the  
35 peak MWEs. Intensification over the continental slope region significantly increases the  
36 currents along the shelf region and coast. The effect on peak maximum depth averaged current  
37 extends up to 400 km from the landfall location. Thus, it is necessary to consider the effect of  
38 various combinations of the highest cyclone intensity and duration of intensification for  
39 identifying the worst scenarios for impact assessment of coastal processes and sediment  
40 transport. The study is quite useful in improving the storm surge prediction, in preparedness,  
41 risk evaluation, and vulnerability assessment of the coastal regions in the present changing  
42 climate.

43 ***Keywords:*** *Tropical Cyclone, Rapid intensification, Gradual intensification, Duration of*  
44 *Intensification, Storm Surge, Hydrodynamics*

## 45 **Declarations**

## 46 **Funding**

47 Industrial Research & Consultancy Centre (07IR001) and Department of Civil Engineering  
48 (DF/1111020) at Indian Institute of Technology (IIT) Bombay.

## 49 **Conflicts of interest/Competing interests**

50 The authors declare that they have no known conflicts of interest/competing interests.

51

## 52 **1. Introduction**

53 Indian ocean is warming at a rapid pace giving rise to increased tropical cyclone (TC) activities  
54 under the changing climate (Singh and Roxy 2020). Storm surge is one of deadliest and  
55 frequently occurring extreme events associated with TCs that affect the coastal community.  
56 TC induced storm surge in the Bay of Bengal (BoB) is reported to be the most destructive in  
57 nature as it affects the socio-economics of the densely populated coastal community India,  
58 Bangladesh, Sri Lanka and Myanmar. The life of a cyclone starts as a tropical disturbance with  
59 lower wind speed that intensifies based on its favourable condition while ends with the cyclone  
60 decaying. A TC is categorised based on upper bound of the highest maximum sustained wind  
61 speed during its life cycle. The improvement in the track and the intensity prediction have  
62 resulted in improvement in the surge prediction accuracy as well. But the abrupt variation in  
63 the storm parameters such as cyclone intensity, pressure drop, duration, translation speed,  
64 cyclone track during the life of a TC make the storm surge prediction further challenging in a  
65 changing climate.

66 Cyclone intensity is measured in terms of the maximum sustained wind speed measured for  
67 duration of 1 or 3 or 10 minute over an unobstructed height of 10m. Table 1, shows the cyclone  
68 category based on the India Meteorological Department (IMD), with the maximum sustained  
69 wind speed measured for a duration of 3 minutes. Intensification rate of a cyclone is computed  
70 by forward differencing the maximum sustained surface wind speed in time, usually at a 6-  
71 hour interval (Mei et al. 2012). A rapidly intensifying cyclone refers to those cyclones whose  
72 wind speed escalates by 15 m/s or more within a period of 24 hours, while those intensified by  
73 less than 15 m/s are referred to as gradually intensifying cyclones. A cyclone undergoes abrupt  
74 variation in the intensity along its path of propagation leading to forecast errors that can affect  
75 the surge response at the coast. The destructive nature of the cyclone wind intensity makes it  
76 practically impossible to measure it directly. In the absences of observations from the surface  
77 ships or instrumented ocean buoys, Dvorak technique (Dvorak 1975) estimates the cyclone  
78 intensity from Infrared and/or satellite imagery based on their appearances, temperature, and  
79 apparent motion of cloud features over time and are represented as Current Intensity (C.I) or  
80 T-number, where T refers to the TC. The minimum T-number of different cyclone category is  
81 shown in Table 1.

82 The extreme sea level rise caused by TC storm surge pose major catastrophic damage to life  
83 and property as a result of coastal inundation, and create an imbalance to the existing coastal

84 ecosystem. Knapp & Kruk (2010) reported variations in the best track information provided by  
85 different agencies that include IMD and JTWC. Their study reports that there exist variations  
86 in the maximum sustained wind speed as well as the temporal scale of the maximum sustained  
87 wind speed. Recent investigations on the cyclone activities under the changing climate, (Elsner  
88 et al. 2008; Balaguru et al. 2014, 2018; Sebastian and Behera 2015; Bhatia et al. 2019; IPCC  
89 2019; Albert and Bhaskaran 2020; Wu et al. 2020) have revealed an increase in the cyclone  
90 intensity, duration, intensifying rate, etc. especially in the Atlantic Ocean and North Indian  
91 Ocean (NIO) regions. Underestimation/overestimation of the cyclone intensity during a TC  
92 event impact the storm surge prediction accuracy. Many researchers (McInnes et al. 2003; Irish  
93 et al. 2008; Rego and Li 2009; Resio et al. 2013; Cyriac et al. 2018; Sahoo and Bhaskaran  
94 2018; Sebastian et al. 2019; Thomas et al. 2019; Li et al. 2020; Poullose et al. 2020) have  
95 quantified the impact of storm surge with changing intensity, storm size, speed of the storm,  
96 approach angles but the impact of duration of the highest cyclone intensity on the storm surge  
97 has not been addressed yet. Though they are expected to result in higher storm surge, the coastal  
98 geometry can alter the storm surge characteristics (Resio and Westerink 2008; Sebastian et al.  
99 2014, 2019). Here an attempt is made to understand the effect of the highest maximum  
100 sustained wind speed of a cyclone and its duration on the storm surge and hydrodynamics.

## 101 **2. Study Area**

102 Compared to the TCs in the world, only 7 % of them occur in NIO but consequences of one  
103 cyclone striking the Indian subcontinent is higher than elsewhere. Storm surge is one of the  
104 known threats associated with TC landfall causing a rise/fall in surface water level near the  
105 coastal area resulting in inland flooding/grounding of vessels. NIO is divided into two basins,  
106 Arabian Sea towards the west and BoB towards the east of the Indian subcontinent. Figure 1  
107 shows the cumulative tracks of the landfalling cyclones from 1970-2019 in NIO. Therefore,  
108 storm surge related vulnerability regions are more along the east coast than the west coast.

109 For the present study, a low lying coast of Andhra Pradesh on the east coast of India, between  
110 Bapatla and Kakinada, holding estuaries of the two major rivers Krishna and Godavari (shown  
111 in Figure 2) is selected for the study. This region belongs to a Very High Risk Zone (VHRZ)  
112 (INCOIS, 2020; Keim et al., 2020; Rao et al., 2007) as per the storm potential vulnerability.  
113 The deltaic plain formed by the two rivers Krishna and Godavari, also widely known as  
114 Krishna-Godavari (K-G) basin is a proven petroliferous basin of continental margin located on  
115 the east coast of India. The K-G basin has a coastline of approximately 300 km and extends

116 offshore up to 1000m isobaths. Directorate General of Hydrocarbon (DGH) of India reports K-  
117 G Basin as an established hydrocarbon province with an oil and gas resource of about 1130  
118 MMT (Million Metric Tons), along both onshore and offshore locations (DGH 2015). About  
119 555 MMT are assessed for the offshore region up to 200 m isobaths.

120 The Cyclone eAtlas-IMD (2020), reports 24 CS or more intense storms along the Andhra  
121 Pradesh coast from 1982-2020 out of which 8 made landfall along the coast of K-G basin. The  
122 coastal region of K-G basin consists of complex geomorphologic units like upland plains,  
123 coastal plains, recent flood and delta plains that are low lying and with gentle slope (DGH  
124 2015) making storm surge prediction challenging in this region. For offshore platform  
125 constructions, the American Petroleum Institute (API 2003) recommends design criteria based  
126 on a 100 year return period storm event. The design water level is a combination of tide, storm  
127 surge and wave set up due to a 100-year return period storm event. But before designing the  
128 water level, it is necessary to define worst-case scenarios during risk evaluation or impact  
129 assessment studies. Previous studies carried out along the K-G basin includes, the impact of  
130 rising sea level along the low lying region of the K-G basin (Rao et al., 2008), storm surge  
131 inundation studies resulting from 1989 Kavali Cyclone and 1996 Andhra Cyclone (Rao et al.,  
132 2013), shoreline changes due to change in climate over the K-G basin (Kallepalli et al. 2017).  
133 Previous studies (Jain et al., 2010; Sindhu & Unnikrishnan, 2012) that computed the expected  
134 total water level with a return period of 50 years along the east coast of India found the low-  
135 lying area of the Krishna River prone to expected total water level of  $6.0 \pm 0.4$  m. The K-G  
136 basin is a micro-tidal region with a tidal range less than 1.5 m and significant wave height less  
137 than 2 m (Rao et al., 2008). Sebastian & Behera (2018) studied the storm surge and current  
138 response along the K-G basin due to SCS events *Laila* (2010) and *Helen* (2013), approaching  
139 at two different angles making landfall closer to each other, reportedly generating a maximum  
140 storm surge height of 1m and maximum currents of 1.2 m/s along the coast.

### 141 **3. Data and Methodology**

142 Based on the IMD and JTWC best track archives of TC, a preliminary assessment of  
143 concerning highest cyclone intensity, duration sustained and their distance to the landfall of  
144 BoB cyclones is carried out. The JTWC provides the best track of cyclones in NIO from 1945  
145 to 2018 (JTWC 2020), whereas the best tracks of cyclone from IMD are available only from  
146 1982. Thus, on comparing the frequency cyclone events in BoB from 1982-2018, it could be  
147 identified that JTWC reported 6 cyclones less when compared to the IMD. On investigating

148 further, it could be found that two of them belong to ESCS, and originated in the Gulf of  
149 Thailand and belonged to the JTWC best track archives of Western North Pacific Ocean. The  
150 highest cyclone intensity and its durations of the landfalling cyclones, formed in BoB from  
151 IMD and JTWC best track archives are shown in Figure 3. Variation in the intensity and  
152 duration of the maximum sustained wind speed from the two different agencies can be  
153 explicitly observed from Figure 3. This instigates a need to understand the effect of highest  
154 cyclone intensity and duration on the storm surge behavior.

155 Figure 4(a) represents the highest cyclone intensity, duration sustained and its closeness to the  
156 landfall time of TCs from 1982-2020 obtained from IMD best tracks. It is observed that 34  
157 (~38%) TC events made landfall with their highest cyclone intensity, 46 (~52%) TCs dissipated  
158 within 24 hours to landfall. Similar to the sustained duration, the distance travelled by highest  
159 cyclone intensity and their closeness to the landfall location estimated from the best tracks of  
160 IMD from 1982-2020 (up to May) is shown in Figure 4(b). On examining Figure 4(b), it could  
161 be found that about 80% of cyclones' highest intensity decays within 200 km to landfall  
162 location. In Figure 4(a) the circles represent the cyclones with their highest intensity only at a  
163 given time (22 such events reported from 1982-2020). Similarly, the circles in Figure 4(b)  
164 represent the cyclone highest intensity at a given time (22 TCs) as well as those intensified  
165 over a duration but remained stationary (5 TCs) for some duration but reduced their intensity  
166 as they move towards the land.

167 In the present study, we have only considered the impact of cyclones with maximum sustained  
168 wind speed higher than 33 m/s during its lifetime. On inspecting the historical cyclone tracks  
169 we come to an understanding that about 90% of the cyclones intensify and dissipate within 24  
170 hours to the landfall time. Hence, for the numerical experiments the cyclone intensities are  
171 increased at 24 hours or lesser duration to the landfall time. To quantify the effect of cyclone  
172 intensity and its duration a single cyclone track is only considered for the present study. For  
173 understanding the impact caused by the change in the cyclone intensity and duration, a cyclone  
174 track from the best tracks is selected and the maximum sustained wind speed of the cyclone  
175 are increased by 2.57 m/s(5 knots), 5.14 m/s(10 knots), 7.71 m/s(15 knots), 15.4 m/s(30 knots)  
176 and 30.86 m/s(60 knots) for 10 different test scenarios for which the cyclone intensities are  
177 increased for varying durations as shown in Figure 5. The central pressure values were also  
178 updated corresponding to the increased maximum sustained wind speed according to the  
179 information available from the best tracks. The experiments were conducted using *Laila*  
180 *Cyclone* that made landfall as a SCS at Bapatla, on May 20<sup>th</sup>, 2010, 1200 UTC. The increased

181 cyclone intensity resulted in changes in the maximum sustained wind speed, minimum central  
 182 pressure and the radius of the maximum winds. Table 2 shows the total numerical experiments  
 183 conducted for the analysis.

### 184 **3.2 Numerical Model**

#### 185 **3.2.1 ADCIRC**

186 ADCIRC solves the shallow water equations (SWE) on unstructured meshes using continuous-  
 187 Galerkin finite element method with linear  $C_0$  triangular elements, allowing localized  
 188 refinement in the region where the solution gradients are largest. The time derivative for the  
 189 continuity equation is discretised over three levels such that the future water level requires  
 190 information on the present and past water levels. In the case of momentum equation, the  
 191 temporal discretization is explicit for all terms except the Coriolis, which uses an average of  
 192 present and future velocities. ADCIRC solves for the water level and two components of  
 193 currents at every mesh node at each time step over the simulation duration.

194 ADCIRC computes the water level from the solution of Generalized Wave Continuity Equation  
 195 (GWCE) that is a combined form of the continuity and momentum equations, whereas the  
 196 currents are computed from the solution of the vertically integrated momentum equations.

197 The generalized wave continuity equation is

$$\frac{\partial^2 \zeta}{\partial t^2} + \tau_0 \frac{\partial \zeta}{\partial t} + S_p \frac{\partial \tilde{J}_\lambda}{\partial \lambda} + \frac{\partial \tilde{J}_\phi}{\partial \phi} - S_p UH \frac{\partial \tau_0}{\partial \lambda} - VH \frac{\partial \tau_0}{\partial \phi} = 0 \quad (1)$$

where,

$$\begin{aligned} \tilde{J}_\lambda = & S_p Q_\lambda \frac{\partial U}{\partial \lambda} - Q_\phi \frac{\partial U}{\partial \phi} + f Q_\phi - \frac{g}{2} S_p \frac{\partial \zeta^2}{\partial \lambda} - g S_p H \frac{\partial}{\partial \lambda} \left[ \frac{P_s}{g \rho_0} - \alpha \eta \right] + \frac{\tau_{s\lambda, winds} + \tau_{s\lambda, waves} - \tau_{b\lambda}}{\rho_0} \\ & + (M_\lambda - D_\lambda) + U \frac{\partial \zeta}{\partial t} + \tau_0 Q_\lambda - g S_p H \frac{\partial \zeta}{\partial \lambda} \end{aligned}$$

$$\begin{aligned} \tilde{J}_\phi = & S_p Q_\lambda \frac{\partial V}{\partial \lambda} - Q_\phi \frac{\partial V}{\partial \phi} + f Q_\lambda - \frac{g}{2} \frac{\partial \zeta^2}{\partial \phi} - g H \frac{\partial}{\partial \phi} \left[ \frac{P_s}{g \rho_0} - \alpha \eta \right] + \frac{\tau_{s\lambda, winds} + \tau_{s\lambda, waves} - \tau_{b\phi}}{\rho_0} \\ & + (M_\phi - D_\phi) + V \frac{\partial \zeta}{\partial t} + \tau_0 Q_\phi - g H \frac{\partial \zeta}{\partial \phi} \end{aligned}$$

198 The vertically integrated momentum equations are

$$\begin{aligned}
\frac{\partial U}{\partial t} + S_p U \frac{\partial U}{\partial \lambda} + V \frac{\partial U}{\partial \phi} - fV \\
= -gS_p \frac{\partial}{\partial \lambda} \left[ \frac{p_s}{g\rho_0} + \zeta - \alpha\eta \right] + \frac{\tau_{s\lambda,winds} + \tau_{s\lambda,waves} - \tau_{b\lambda}}{\rho_0 H} \\
+ \frac{M_\lambda - D_\lambda}{H}
\end{aligned} \tag{2}$$

$$\begin{aligned}
\frac{\partial V}{\partial t} + S_p U \frac{\partial V}{\partial \lambda} + V \frac{\partial V}{\partial \phi} - fU \\
= -g \frac{\partial}{\partial \phi} \left[ \frac{p_s}{g\rho_0} + \zeta - \alpha\eta \right] + \frac{\tau_{s\phi,winds} + \tau_{s\phi,waves} - \tau_{b\phi}}{\rho_0 H} \\
+ \frac{M_\phi - D_\phi}{H}
\end{aligned} \tag{3}$$

199 where, t = time,

200  $H = \zeta + h$  = the total water depth,

201  $\zeta$  = the deviation of the water surface from the mean water level,

202  $h$  = bathymetric depth;

203  $\lambda$  = degrees longitude (east of Greenwich is positive) and

204  $\phi$  = degrees latitude (north of equator is positive)

205  $S_p = \cos \phi_0 / \phi$ , is a spherical co-ordinate conversion factor and  $\phi_0$  is a reference latitude.

206  $U, V$  = the depth-averaged horizontal velocities in x- and y-directions, respectively,

207  $Q_\lambda = UH$ , and  $Q_\phi = VH$ , are fluxes per unit width in x- and y-directions, respectively,

208  $f = 2\Omega \sin\phi$  = the Coriolis parameter,

209  $\Omega$  = the angular speed of the earth,

210  $P_s$  = the atmospheric pressure at free surface,

211  $g$  = acceleration due to gravity,

212  $\eta$  = the Newtonian equilibrium tidal potential,

213  $\alpha$  = the effective earth elasticity factor,

214  $\rho_0$  = the reference density of water,

215  $\tau_{s,winds}, \tau_{s,waves}$  = the applied free surface stress due to winds and waves, respectively,

216  $\tau_b$  = bottom stress ,

217  $M_\lambda, M_\phi$  are lateral stress gradients,

218  $D_\lambda, D_\phi$  are momentum dispersion terms

219  $\tau_0$  is a numerical parameter that optimizes the phase propagation properties (Kolar et al. 1994;  
220 Atkinson et al. 2004)

221 ADCIRC utilizes the mass conservation in the depth-integrated form of Generalized Wave-  
222 Continuity Equation (GWCE) and the momentum conservation subjected to incompressibility.  
223 Additionally, equations of motion in the ADCIRC model are formulated based on the  
224 traditional hydrostatic pressure, Boussinesq approximations. The GWCE formulation  
225 developed by Lynch & Gray (1979) eliminate the spurious node-node oscillations associated  
226 with a primitive Galerkin finite element formulation of the vertically-integrated continuity  
227 equation. The model utilizes FEM for spatial discretisation and FDM for temporal  
228 discretisation. ADCIRC uses a linear Lagrange interpolation to solve for the water levels ( $\zeta$ )  
229 and velocities ( $U$  and  $V$ ) at every node point of the unstructured triangular mesh. The GWCE  
230 can use explicit or implicit time stepping scheme. The momentum equation uses a consistent  
231 or lumped mass matrix. The 2DDI form uses the explicit time stepping scheme and in order to  
232 avoid the instability in the computation a suitable time step was selected to satisfy the Courant–  
233 Friedrichs–Lewy (CFL) (Courant et al. 1928) stability criteria.

### 234 3.2.2 SWAN

235 SWAN is a third generation wave model that simulates the nearshore waves (Booij et al. 1999)  
236 that represents the wave field as phase averaged spectrum. The wave action density,  
237  $N(t, \lambda, \phi, \sigma, \theta)$  is allowed to evolve in time ( $t$ ), geographic space ( $\lambda, \phi$ ) and spectral space  
238 (relative frequencies  $\sigma$  and directions  $\theta$ ). The governing action balance equation is

$$\frac{\partial N}{\partial t} + \frac{\partial}{\partial \lambda} [(c_\lambda + U)N] + \cos^{-1} \phi \frac{\partial}{\partial \phi} [(c_\phi + V)N \cos \phi] + \frac{\partial}{\partial \theta} [c_\theta N] \quad (4)$$

$$+ \frac{\partial}{\partial \sigma} [c_{\sigma} N] = \frac{S_{tot}}{\sigma}$$

239 where,  $c_{\lambda}$ ,  $c_{\phi}$  are the group velocities; U, V are the ambient current;  $c_{\theta}$ ,  $c_{\sigma}$  are the propagation  
 240 velocities in  $\theta$ - and  $\sigma$ - spaces;  $S_{tot}$  is wave growth by wind action lost due to white capping,  
 241 surf breaking and bottom friction and action exchanged between spectral components due to  
 242 nonlinear effects in deep and shallow water.

243 The radiation stress gradients are computed by

$$\tau_{sx,waves} = -\frac{\partial S_{xx}}{\partial x} - \frac{\partial S_{xy}}{\partial y} \quad (5)$$

$$\tau_{sy,waves} = -\frac{\partial S_{xy}}{\partial x} - \frac{\partial S_{yy}}{\partial y} \quad (6)$$

244 where,  $S_{xx}$ ,  $S_{xy}$ , and  $S_{yy}$  are the wave radiation stresses (Longuet-Higgins and Stewart 1964;  
 245 Battjes 1972) and are given as:

$$S_{xx} = \rho_0 g \iint \left( \left( n \cos^2 \theta + n - \frac{1}{2} \right) \sigma N \right) d\sigma d\theta \quad (7)$$

$$S_{xy} = \rho_0 g \iint (n \sin \theta \cos \theta \sigma N) d\sigma d\theta \quad (8)$$

$$S_{yy} = \rho_0 g \iint \left( \left( n \sin^2 \theta + n - \frac{1}{2} \right) \sigma N \right) d\sigma d\theta \quad (9)$$

246 where, n is the ratio of group velocity to phase velocity.

247 Zijlema (2010) introduced a numerical procedure to compute the wind-wave spectra using  
 248 SWAN on unstructured-grid. A vertex based, fully implicit, finite difference method  
 249 accommodated the unstructured meshes with high variability associated with bathymetry in the  
 250 nearshore region and irregular shoreline. A point to point multi-directional Gauss-Seidel  
 251 iteration method requiring a number of sweeps through the grid was adopted for the numerical  
 252 solution method. The implicit time scheme permitted stability in the computation even in case  
 253 of local refinement in the area of interest.

### 254 3.2.3 Coupled ADCIRC+SWAN

255 A coupled wave and circulation model can define shelf, nearshore and inland hydrodynamics  
 256 better during a cyclone event. The wave effects are incorporated in the circulation model by

257 parallelly coupling the third generation wave model, SWAN with ADCIRC(Dietrich et al.  
258 2012). The unstructured-mesh SWAN spectral wave model and the ADCIRC shallow-water  
259 circulation model have been integrated into a tightly-coupled ADCIRC + SWAN model.

260 The tight coupling of the unstructured SWAN model and ADCIRC allows physical interaction  
261 between the wave-circulation to be resolved correctly in both models. ADCIRC passes wind  
262 velocities, water levels, and currents through local memory to SWAN, which is utilized for its  
263 computation. SWAN computes wave radiation stresses and their gradients and passes radiation  
264 stress gradients as a forcing function to ADCIRC at the end of each its time steps. ADCIRC  
265 time step is relatively small in order to satisfy the Courant number criteria of its explicit features  
266 as well as to limit the propagation speed of wetting front during a time step. Whereas, SWAN  
267 is unconditionally stable and allows large time steps. Thus, the coupling interval is the same as  
268 the SWAN time step. The models are run sequentially to ensure that either ADCIRC or SWAN  
269 runs alternatively passing information to each other (Dietrich et al. 2011, 2012).

270 At the beginning of the coupling interval ADCIRC can access the radiation stress gradient  
271 computed by SWAN at times corresponding to the beginning and end of the previous interval.  
272 At the end of the coupling time interval, ADCIRC passes the wind velocities, water levels,  
273 currents and roughness lengths to SWAN. SWAN recalculates the water depth and related  
274 wave process (wave propagation, depth-induced breaking, etc.) at the coupling time. SWAN is  
275 run for the same time step to bring the same moment in time as ADCIRC. The radiation stresses  
276 are computed at each mesh node and are interpolated into the space of continuous, piecewise  
277 linear functions and differentiated to obtain the radiation stress gradient that is constant on each  
278 element. The area-weighted average of the radiation stress gradient on the element is projected  
279 onto the mesh nodes. The radiation stress gradients used by ADCIRC are always extrapolated  
280 forward in time, while the wind speed, water levels and currents used by SWAN are always  
281 averaged over each of its time step (Dietrich et al. 2011).

282 ADCIRC and SWAN are run in parallel mode for the present study. ADCIRC and SWAN have  
283 a one-to-one correspondence between geographic locations of the mesh vertices as they use the  
284 same local sub-mesh. Information such as water level, currents, wind velocities and radiation  
285 stress gradients are passed directly through the local cache or memory, without any need for  
286 interpolation.

### 287 3.3 Generating the Wind field and Pressure Field

288 Holland et al. (2010) proposed a revision to the parametric Holland (1980) model to represent  
 289 the surface wind profile more accurately. The earlier model utilized the central and  
 290 environmental surface pressure, maximum winds and radius of maximum wind, while the  
 291 revised model is capable of incorporating the wind observations at some radius within the  
 292 hurricane circulation. The revised model is considerably less sensitive to data errors. The  
 293 surface pressure  $P_s$  is given by

$$P_s = P_{cs} + (P_{ns} - P_{cs})e^{-\left(\frac{R_m}{r}\right)^b} \quad (10)$$

294 where,  $P_s$  is surface pressure at radius  $r$ ,  $P_{cs}$  is central pressure,  $P_{ns}$  is the external pressure to  
 295 the centre of the cyclone,  $R_m$  is the radius of maximum winds.  $b$  is the scaling parameter that  
 296 defines the proportion of pressure gradient near the maximum wind,  $e$  is the exponential  
 297 function.

$$V_s = V_{ms} \left\{ \left( \frac{r_{v_{ms}}}{r} \right)^{b_s} e^{\left[ 1 - \left( \frac{r_{v_{ms}}}{r} \right)^{b_s} \right] x} \right\} \quad (11)$$

298 where,  $V_s$  = surface wind (wind at any level),  $V_{ms}$  = maximum surface wind,  $r_{v_{ms}}$  is the radius  
 299 of maximum wind,  $b_s = b g_s^x$ , where,  $g_s$  is the reduction factor for gradient to surface winds,  $e$  is  
 300 the base of natural logarithm. Based on the central pressure value,  $b_s$  is obtained as follows;

$$b_s = -4.4 \times 10^{-5} \Delta P_s^2 + 0.01 \Delta P_s + 0.03 \frac{\partial P_{cs}}{\partial t} - 0.014 \phi + 0.15 V_t^x + 1.0 \quad (12)$$

$$x = 0.5 \left( 1 - \frac{\Delta P_s}{215} \right) \quad (13)$$

$$V_{ms} = \left( \frac{100 b_s \Delta P_s}{\rho_{ms} e} \right)^{0.5} \quad (14)$$

301 where,  $\Delta P_s$  is in hPa,  $\partial P_{cs}/\partial t$  intensity change in hPa/h,  $\phi$  is the absolute value of latitude in  
 302 degree,  $V_t$  is the cyclone translate speed in m/s.

303 The surface air density can be derived as

$$\rho_s = \frac{100 P_s}{R T_{vs}}, \quad (15)$$

$$T_{vs} = (T_s + 273.15)(1 + 0.61 q_s)$$

$$q_s = RH_s \left( \frac{3.802}{100P_s} \right) e^{\frac{17.67T_s}{243.5+T_s}}$$

$$T_s = SST - 1$$

304 where,  $R=286.9 \text{ J kg}^{-1}\text{K}^{-1}$  is the gas constant for dry air,  $T_{vs}$ = the virtual surface temperature  
 305 (in K),  $q_s$  is the surface moisture (in  $\text{g kg}^{-1}$ ),  $T_s$ = surface temperature, SST is the sea surface  
 306 temperature (both in  $^{\circ}\text{C}$ ),  $RH_s$ = surface relative humidity.

307 The radius of maximum wind is computed using Willoughby & Rahn (2004) equation given  
 308 by

$$R_m = 46.4e^{(-0.0515V_m+0.0169\phi)} \quad (16)$$

309 The storm parameters (track positions, maximum sustained wind speeds and estimated  
 310 pressures) obtained from the JTWC best track for cyclones Hudhud, Helen and Laila to  
 311 compute their respective wind and pressure fields from this modified Holland Model (MHM).  
 312 The radius of the maximum winds are computed using the Willoughby & Rahn (2004)  
 313 equation. For the numerical experiments the radius of maximum winds varies based on the  
 314 wind speed and is as shown in Figure 6. Further, for the numerical experiments, adopting the  
 315 track positions of Laila Cyclone maximum sustained wind speeds and the minimum central  
 316 pressures are varied at selected time instances as shown in Figure 7. These wind and pressure  
 317 information are interpolated in space onto the ADCIRC grid and in time to match the wind and  
 318 pressure information with the model time step. The wind drag coefficients are adopted from  
 319 Garratt(1977) for all the simulations.

### 320 **3.4 Model Set up and Initialization**

321 The numerical simulations are carried out using standalone model ADCIRC and coupled model  
 322 ADCIRC+SWAN on the domain consisting of the BoB basin of NIO. The model domain is  
 323 discretised into highly flexible unstructured mesh as shown Figure 8. The model domain  
 324 consists of 85,371 triangular elements and 459,419 nodes, with a resolution of 100 m along the  
 325 east coast of India. However, the coastal belt of this region is low lying with gentle slopes and  
 326 is categorized as highly vulnerable to storm surge (Kallepalli et al. 2017). Figure 9(a) shows  
 327 BoB model domain with interpolated bathymetry from GEBCO. Figure 9(b) shows the  
 328 enlarged view of the K-G basin. Before conducting the numerical experiment, the model is  
 329 validated with the water levels obtained at Visakhapatnam and Krishnapatnam during *Helen*

330 (2013), which made landfall as a SCS as well as the water levels obtained at Visakhapatnam  
331 during *Hudhud* (2014) that made landfall as an ESCS. In Figure 9, in addition to the  
332 bathymetry, the cyclone tracks of *Laila*, *Helen* and *Hudhud* are also incorporated. The landfall  
333 locations as well as the tide gauge stations are shown in the enlarged view of the study area  
334 (Figure 9(b)).

335 Boundary conditions used in the present simulations include mainland boundary and islands  
336 with no normal flow condition and free tangential slip and open ocean boundary with specified  
337 tidal constituents for harmonic forcing. The meteorological forces comprising the wind and  
338 pressure field during cyclone events of *Hudhud*, *Helen* and *Laila* are computed from the MHM.  
339 In addition to the boundary conditions, an elemental wetting-drying scheme with minimum  
340 water depth 0.05 m and a minimum velocity of 0.05 m/s is adopted. A constant bottom friction  
341 coefficient of 0.0028 that uses the quadratic friction formulation is used for bottom friction  
342 parameterisation. The time step of 6 s satisfied the Courant number criteria.

343 The model is initially run for 60 days in cold start with tidal forcing and potential constituents  
344 obtained from Le Provost database allowing 20 days for the model to spin up. The numerical  
345 simulation is forced with all 13 forcing and potential tidal constituents ( $2N_2$ ,  $K_1$ ,  $K_2$ ,  $L_2$ ,  $M_2$ ,  
346  $MU_2$ ,  $N_2$ ,  $NU_2$ ,  $O_1$ ,  $P_1$ ,  $Q_1$ ,  $S_2$ ,  $T_2$ ) at the open ocean boundary. The simulation is initialised  
347 with tidal potential forcing. Further, simulations are carried out hot starting the computational  
348 domain with meteorological forcing for another 5 days (life of *Laila* Cyclone).

## 349 **4. Results and Discussion**

350 The simulations carried out using the ADCIRC model considers the effect of atmospheric  
351 forcing of a cyclone along with tide are referred to as storm tide (ST) conditions. Similarly,  
352 simulations carried out using ADCIRC+SWAN model consider the effect of wave setup along  
353 with the storm tide and are referred to as storm-tide-wave (STW) conditions in the following  
354 sections.

### 355 **4.1 Validation of water level**

356 The water levels simulated during *Helen* cyclone is compared with the tide gauge observations  
357 at Visakhapatnam and Krishnapatnam obtained from INCOIS and is shown in Figure 10. It is  
358 seen the numerical model slightly under predicts the amplitude of the water levels but the phase  
359 is in good agreement with each other. The observed water levels are recorded by the tide gauge

360 station located inside the Visakhapatnam port, whereas, the numerical model point lies in the  
361 open coast without considering the port enclosure. Also, the numerical model used GEBCO  
362 bathymetry only. The results might further improve by considering more refined bathymetry  
363 information from hydrographic charts for the K-G basin region. Further, the water levels  
364 simulated during an ESCS *Hudhud* Cyclone are compared with the tide gauge observations at  
365 Visakhapatnam, where the cyclone made its landfall and are shown in Figure 11. The model  
366 could capture the amplitude as well as phase of the total water level using the coupled  
367 ADCIRC+SWAN model with a CC value of 0.98 and RMSE of 0.02 m.

#### 368 **4.2 Maximum Wind Speed and Minimum Pressure**

369 In the present study, to investigate the impact of intensification on the coastal storm surge,  
370 cyclones are intensified gradually by increasing the maximum sustained wind speed by 2.57  
371 m/s (5 knots), 5.14 m/s (10 knots) and 7.71 m/s (15 knots) as well as rapidly by 15.4 m/s (30  
372 knots) and 30.86 m/s (60 knots) for 10 hypothetical different durations. The maximum  
373 sustained wind speed and pressure variation during the life of the cyclone are presented in  
374 Figure 7, which are used for generating the wind fields in the numerical simulations. With  
375 respect to the change in the wind speed there will be change in the radius of maximum winds  
376 as well. The radius of maximum winds corresponding to the maximum sustained wind speed  
377 is shown in Figure 6. When the cyclones are intensified, changes occur in wind speed, pressure  
378 as well as in the radius of maximum wind of the cyclone. The spatial distribution of the  
379 maximum wind speed during *Laila* Cyclone and for increased intensities of test scenario A  
380 (where the cyclone intensity was increased 24 hours prior to landfall and 6 hours after landfall  
381 as shown in Figure 5) is shown in Figure 12. Since the highest maximum sustained wind speeds  
382 are increased by 5, 10, 15, 30 and 60 knots, they are designated as A5, A10, A15, A30 and  
383 A60, respectively. Similarly, the spatial distributions of minimum pressure experienced during  
384 *Laila* Cyclone and for increased intensities of test scenario A are shown in Figure 13.

385 From Figure 12, we can see that with an increase in wind speed by 2.57 m/s (5 knots), the  
386 highest wind speed of A5 (Figure 12(b)) increases by 0.5 m/s of *Laila* Cyclone (Figure 12(a)).  
387 The increased wind speed between 24-32 m/s, closer to the landfall, belongs to SCS. While  
388 with an increase of 5.14(10), 7.71(15) m/s(knots), as seen in Figure 12(c) and (d), the maximum  
389 wind speed near the landfall changed to VSCS category. Similarly, an increase in the wind  
390 speed by 15.4 (30) and 30.86(60) m/s(knots), seen in Figure 12(e) and (f), resulted in ESCS  
391 and SuCS (62.4 m/s).

392 Spatial plots of maximum wind speed with 30.86 m/s (60 knots) increase for different test  
393 scenarios (A – J) representing varying durations are shown in Figure 14(a-j). Similarly, the  
394 corresponding minimum pressures are shown in Figure 15(a-j). The highest wind speed for  
395 Cyclone *Laila* is 34 m/s whereas the lowest pressure value is 9.94 m of water. The highest  
396 maximum wind speeds and the lowest central pressures for all the test scenarios considered for  
397 the study are provided in

398  
399 Table 3.

400 From  
401

402 Table 3, it could be seen that the highest maximum wind speed and lowest minimum pressure  
403 values are same for A, B, C, D, E scenarios because the highest intensification of *Laila* Cyclone  
404 occurred 24 hours prior to landfall that is captured by all these scenarios. For other scenarios,  
405 the highest maximum wind speed and lowest minimum pressure values vary depending on the  
406 specific time instance considered. Sensitivity of the duration and intensity on the maximum  
407 water levels and significant wave heights are investigated using the wind and pressure fields  
408 of different scenarios.

#### 409 **4.3 Maximum Water Elevation (MWE)**

410 The MWE refers to the peak values of water levels obtained throughout the computational  
411 domain for the total period of simulation considered for the study. The MWEs are computed  
412 for ST conditions using ADCIRC model, where cyclonic surge is simulated along with tide.  
413 Similarly, MWEs are also computed for STW conditions using ADCIRC+SWAN model to  
414 consider the effect of wave setup along with storm tide.

415 The peak MWE of ST and STW are computed for all the test scenarios and are shown in Figure  
416 16. The peak MWEs of STW increase up to 39 % of peak MWEs of ST for varying cyclone  
417 intensity and duration of intensification considered here. The peak MWEs are recorded at  
418 different locations for different scenarios and selected locations of peak MWEs are shown in  
419 Figure 17 along with the bathymetric depth. The farthest peak MWE is observed north of  
420 Machilipatnam (~90 km from landfall). As seen in Figure 5, the intensifications are considered  
421 over a duration (A-E) and at specific time instances (F-J). The scenarios B-F, C-G, D-H and  
422 E-I are paired together as their intensification ends at the same time. The comparison of the  
423 peak MWEs among these paired scenarios is done to understand the impact of duration of  
424 intensification. The MWE obtained for *Laila* Cyclone (highest maximum sustained wind

425 intensity of 34 m/s occurred 30 hours prior to the landfall) is also plotted along with the  
426 scenarios to compare and understand the effect of intensification and duration.

427 From Figure 16 it could be concluded that the duration of intensification is trivial. The peak  
428 MWE of STW in the K-G basin with 30.86 m/s (60 knots) increase in intensity shows 10.8%,  
429 17.8%, 1.4% and 14.7% higher MWEs for B, C, D and E scenarios compared to F, G, H and I  
430 scenarios, respectively. In order to understand the impact of the intensification, percentage  
431 increase in the peak water levels of STW with respect to that of *Laila* is estimated and is  
432 provided in

433 Table 4. As explained earlier, an increase in wind speed by 2.57, 5.14, and 7.71 m/s results in  
434 gradual intensification and an increase in wind speed by 15.4, 30.86 m/s results in rapid  
435 intensification (>15 m/s change within 24 hours) of the cyclone. The scenario A where the  
436 intensification continued even after landfall shows substantial increase in the MWEs with  
437 increasing intensities. Similarly, scenarios B, C, F, and G show significant increase in MWEs  
438 for increasing intensities. However, scenarios D and H show considerable increase for rapid  
439 intensification only. Scenarios E and I show an increase in MWEs for an increase of 30.86 m/s  
440 only below which the effect is negligible.

441 In the above discussion, it should be noted that the intensification in these scenarios ends at  
442 different positions of cyclones where the water depths are also varying. As we observe, the  
443 scenarios B, C, F, and G intensification continued over the shallow continental shelf region,  
444 where the bathymetry is less than 200m (seen in Figure 9(b)). Whereas, the scenarios D and H  
445 intensifications happened up to the continental slope (500-2000 m) and scenarios E and I  
446 intensifications were limited to deeper water regions beyond the continental slope (~3000 m).  
447 Now referring to

448 Table 4, it can be concluded that intensification over shallow continental shelf regions has  
449 significant effect on the MWEs. Similarly, intensification in deeper water regions beyond  
450 continental slope has minimal effect on MWEs for gradual intensification but considerable  
451 effect for rapid intensification. The scenario J where the intensification takes place in deep  
452 water (> 3000 m) 24 hours prior to landfall shows insignificant effect on the MWEs along the  
453 coast. Overall, we could conclude that an intensification on shallower regions results in higher  
454 MWEs along the coast for both gradual and rapid intensification. On the contrary, a rapid  
455 intensification in deep water regions can affect the MWEs along the coast but not a gradual  
456 intensification.

457 Although the analysis of peak MWEs has been discussed, it is prudent to investigate the spatial  
458 variation of MWEs along the coast. The spatial contours of MWEs for the extreme case with  
459 30.86 m/s (60 knots) intensification are presented in Figure 18 along with the base case of *Laila*  
460 Cyclone. The scenarios B and F with the same intensity have different duration of

461 intensification. For scenario B, where the intensification happens over duration, the extent of  
462 MWEs along the coast is larger compared to that of scenario F with specific time  
463 intensification. This difference in the extent of influence is mainly due to the locations of  
464 intensification. As in scenario B the intensification happened even farther away from the coast,  
465 the generated surge could reach a wider stretch of the coast. While in scenario F, the effect of  
466 intensification is restricted to a smaller stretch of the coast. Similarly, the location of  
467 intensification also influences the location of MWE along the coast. The spatial MWEs for  
468 scenario J60 and *Laila* are similar without much variation as seen in Figure 18(j) and (k),  
469 respectively. Therefore, the intensification before 24 hours of landfall does not affect the  
470 overall surge characteristics along the coast.

471 It was also observed that the locations of peak MWEs for ST and STW cases do not occur at  
472 the same locations for all scenarios (as seen in Figure 18). The MWEs of ST are subtracted  
473 from STW simulation to obtain the contribution of wave setup and are shown in Figure 19.  
474 Figure 19(a) shows the peak MWEs due to storm tide and wave setup contribution at locations  
475 where the peaks were recorded during STW simulations. Similarly, Figure 19(b) shows the  
476 values from coupled STW simulations but at locations where the peaks were recorded during  
477 ST simulations. This helps to understand the wave setup contribution and its effect at various  
478 locations along the coast. Figure 19(a) shows locations where the storm tide component is zero  
479 signifying that these locations were not inundated when only storm tide simulations were  
480 carried out. However, Figure 19(b) shows less wave setup contribution and more storm tide  
481 contribution at locations where peak MWEs were observed during ST simulations. Hence,  
482 coupled STW modelling is necessary to accurately assess the vulnerability of coastal regions  
483 due to cyclones.

484 The results for scenario A60 show a substantial increase in the ST and STW values. The tidal  
485 range at this location is 0.4 – 0.6 m, which means the surge and wave setup contribution is  
486 highest. To understand the local process and STW amplification, the wind field around the  
487 region and maximum water elevations are shown in Figure 20. It can be seen that this location  
488 has a coastal profile with high curvature and can trap the flow without much escape of flux.  
489 This could lead to piling of water resulting in very high MWE, emphasizing the importance of  
490 coastal geometry on the resultant flooding and inundation.

#### 491 4.4 Maximum Depth Averaged Current ( $V_{avg\_max}$ )

492 The depth averaged velocities ( $V_{avg}$ ) are obtained from the coupled model, and the  $V_{avg\_max}$   
493 refers to the highest  $V_{avg}$  in the computational domain during the considered simulation period.  
494 The peak  $V_{avg\_max}$  for *Laila* cyclone is 5.4 m/s, while for different test scenarios the peak  
495  $V_{avg\_max}$  is given in Table 5. On the first hand observation, it can be seen that the peak  $V_{avg\_max}$   
496 has increased for all scenarios with rapid intensification. However, the same is not seen in case  
497 of gradual intensification and with 2.54 (5) and 5.14 (10) m/s (knots) increase, most scenarios  
498 show reduced peak  $V_{avg\_max}$ . In case of 7.71 m/s (15 knots) increase, scenarios A, B, C, D, H,  
499 and I show increased peak  $V_{avg\_max}$ . A closer look suggests that an increase in average velocity  
500 magnitude is observed where the gradual intensification takes place over the continental slope  
501 region (where bathymetric gradient is very high). For gradually intensifying cyclones, a  
502 variation in the peak  $V_{avg\_max}$  up to 11% is observed compared to *Laila*. In order to understand  
503 the spatial variation of average velocities, the  $V_{avg\_max}$  with the extreme case (30.86 m/s  
504 intensification) of all scenarios are plotted in Figure 21 along with results of *Laila* cyclone. A  
505 strong velocity field is observed in the shelf region for scenarios A, B, C, and G, whereas, the  
506 magnitude reduces for the scenarios D, E, F, H, I, and J. It is important to note that scenario G  
507 shows similar current magnitudes as of the scenarios A, B, and C, those intensify over duration.  
508 This clearly states that the intensification along the continental slope results in higher currents  
509 along the cyclone path in the shelf region.

510 Although, the increase in current magnitude is less for many scenarios shown in Figure 21(a-  
511 j), it is higher compared to the current magnitudes generated due to *Laila* cyclone (Figure  
512 21(k)). It can be concluded that a rapid intensification of cyclones in deep and shallow water  
513 can result in increased current magnitudes in the shelf region.

514 It is also important to identify the locations of peak  $V_{avg\_max}$  in addition to the increased  
515 magnitude. The locations and bathymetry of the peak  $V_{avg\_max}$  for all the scenarios are shown  
516 in Figure 22. It can be seen that for all simulations, the peak  $V_{avg\_max}$  are recorded along the coast,  
517 which could affect the coastal dynamics and processes during the event. Unlike the peak  
518 MWEs that were influenced up to a distance of ~90 km from the landfall point, the effect on  
519 peak  $V_{avg\_max}$  is wider extending up to ~400 km, mostly on the right side of the landfall point  
520 (seen in Figure 22). Overall, a rapid intensification of cyclones increases the current magnitudes  
521 in the shelf region as well as along the coast. Intensification over the continental slope region  
522 significantly increases the currents along the coast. Thus, it is necessary to consider such

523 intensifying cyclones while assessing the cyclone impact on coastal processes and sediment  
524 transport during such extreme events.

## 525 **5. Conclusions**

526 The present study shows the sensitivity of coastal water levels with respect to increased  
527 cyclonic intensity with different intensification periods. The studies conclude that duration of  
528 intensification is trivial for gradually intensifying cyclones. The duration of intensification  
529 contributes to about 10-18 % change in the water levels when rapidly intensified over the  
530 continental shelf region. Intensification on shallower regions results in higher MWEs along the  
531 coast for both gradual and rapid intensification. On the contrary, in deep water region, only  
532 rapid intensification can affect the peak MWEs and the effect of gradual intensification in deep  
533 water is insignificant on peak MWEs. A rapid intensification before 24 hours to the landfall  
534 does not affect the overall surge characteristics along the coast. Coupled storm-tide-wave  
535 (STW) simulations result up to 39 % increase in peak MWEs compared to storm tide (ST)  
536 simulations. Therefore, a coupled storm surge-tide-wave (STW) modelling should be carried  
537 out to obtain accurate MWEs and its location for identifying vulnerable coastal regions due to  
538 cyclones. Coastal geometry plays an important role in localized amplification of surge  
539 characteristics.

540 A gradually intensifying cyclone over the continental slope region, resulted in a variation in  
541 the peak  $V_{avg\_max}$  is up to 11%. While a rapidly intensifying cyclone in deep and shallow water  
542 regions can increase the current magnitudes in the shelf region as well as along the coast. The  
543 effect on peak  $V_{avg\_max}$  can extend up to ~400 km mostly on the right side of the landfall point.  
544 Thus, it is necessary to consider such intensifying cyclones while assessing the cyclone impact  
545 on coastal processes and sediment transport under extreme events.

## 546 *Acknowledgement*

547 The first author would like to thank the financial support from the Industrial Research &  
548 Consultancy Centre (07IR001) and Department of Civil Engineering (DF/1111020) at Indian  
549 Institute of Technology (IIT) Bombay for carrying out this work. All the simulations were  
550 carried out at the High Performance computing facility at IIT Bombay, hence we also  
551 acknowledge the SpaceTime-2 supercomputing facility at IIT Bombay for the computing time.  
552 We wish to thank the Earth System Science Organization (ESSO)-Indian National Centre for

553 Ocean Information Services (INCOIS), India for providing the observed tide gauge data free  
554 of cost.

## 555 *References*

556 Albert J, Bhaskaran PK (2020) Evaluation of track length , residence time and translational  
557 speed for tropical cyclones in the North Indian ocean. *ISH J Hydraul Eng* 00:1–8.  
558 <https://doi.org/10.1080/09715010.2020.1825124>

559 API (2003) Recommended Practice for Planning , Designing and Constructing Fixed Offshore  
560 Platforms — Working Stress Design

561 Atkinson JH, Westerink JJ, Luettich RA (2004) Two-dimensional dispersion analyses of finite  
562 element approximations to the shallow water equations. *Int J Numer Methods Fluids*  
563 45:715–749. <https://doi.org/10.1002/fld.701>

564 Balaguru K, Foltz GR, Leung LR (2018) Increasing Magnitude of Hurricane Rapid  
565 Intensification in the Central and Eastern Tropical Atlantic. *Geophys Res Lett* 45:4238–  
566 4247. <https://doi.org/10.1029/2018GL077597>

567 Balaguru K, Taraphdar S, Leung LR, Foltz GR (2014) Increase in the intensity of postmonsoon  
568 Bay of Bengal tropical cyclones. *Geophys Res Lett* 41:3594–3601.  
569 <https://doi.org/10.1002/2014GL060197>

570 Battjes JA (1972) Radiation stresses in short-crested waves. *J Mar Res* 30:1-56.

571 Bhatia KT, Vecchi GA, Knutson TR, et al (2019) Recent increases in tropical cyclone  
572 intensification rates. *Nat Commun* 10:1–9. <https://doi.org/10.1038/s41467-019-08471-z>

573 Booij N, Ris RC, Holthuijsen LH (1999) A third-generation wave model for coastal regions 1.  
574 Model description and validation. *J Geophys Res Ocean* 104:7649–7666.  
575 <https://doi.org/10.1029/98JC02622>

576 Courant R, Friedrichs KO, Lewy H (1928) Uber die partiellen differenzgleichungen der  
577 mathematisches. *Math Ann* 100:32–74

578 Cyclone eAtlas-IMD (2020) Tracks of Cyclones and Depressions over North Indian Ocean  
579 (from 1891 onwards). Chennai

580 Cyriac R, Dietrich JC, Fleming JG, et al (2018) Variability in Coastal Flooding predictions due

581 to forecast errors during Hurricane Arthur. *Coast Eng* 137:59–78.  
582 <https://doi.org/10.1016/j.coastaleng.2018.02.008>

583 DGH (2015) Krishna Godavari – Basin NDR - National Data Repository India.  
584 [https://www.ndrdgh.gov.in/NDR/?page\\_id=647](https://www.ndrdgh.gov.in/NDR/?page_id=647)

585 Dietrich JC, Tanaka S, Westerink JJ, et al (2012) Performance of the unstructured-mesh,  
586 SWAN+ ADCIRC model in computing hurricane waves and surge. *J Sci Comput* 52:468–  
587 497. <https://doi.org/10.1007/s10915-011-9555-6>

588 Dietrich JC, Zijlema M, Westerink JJ, et al (2011) Modeling hurricane waves and storm surge  
589 using integrally-coupled, scalable computations. *Coast Eng* 58:45–65.  
590 <https://doi.org/10.1016/j.coastaleng.2010.08.001>

591 Dvorak VF (1975) Tropical Cyclone Intensity Analysis and Forecasting from Satellite  
592 Imagery. *Mon Weather Rev* 103:420–430

593 Elsner JB, Kossin JP, Jagger TH (2008) The increasing intensity of the strongest tropical  
594 cyclones. *Nature* 455:92–5. <https://doi.org/10.1038/nature07234>

595 Garratt JR (1977) Review of Drag Coefficients over Oceans and Continents. *Mon Weather Rev*  
596 105:915–929. [https://doi.org/10.1175/1520-0493\(1977\)105](https://doi.org/10.1175/1520-0493(1977)105)

597 Holland GJ (1980) An Analytic Model of the Wind and Pressure Profiles in Hurricanes. *Mon*  
598 *Weather Rev* 108:1212–1218

599 Holland GJ, Belanger JI, Fritz A (2010) A Revised Model for Radial Profiles of Hurricane  
600 Winds. *Mon Weather Rev* 138:4393–4401. <https://doi.org/10.1175/2010MWR3317.1>

601 INCOIS (2020) What is the vulnerability of our coastline from the point of view of storm surge  
602 potential? In: ESSO- Indian Natl. Cent. Ocean Inf. Serv. (INCOIS), Govt India.  
603 <https://incois.gov.in/portal/Aboutstormsurge.jsp>

604 Intergovernmental Panel on Climate Change (2019) IPCC Special Report on the Ocean and  
605 Cryosphere in a Changing Climate

606 Irish J, Resio D, Ratcliff J (2008) The influence of storm size on hurricane surge. *J Phys*  
607 *Oceanogr* 38:2003–2013. <https://doi.org/10.1175/2008JPO3727.1>

608 Jain I, Rao AD, Jitendra V, Dube SK (2010) Computation of Expected Total Water Levels

609 along the East Coast of India. *J Coast Res* 26:681–687. <https://doi.org/10.2112/08-1170.1>

610 JTWC (2020) North Indian Ocean Best Track Data. In: Jt. Typhoon Warn. Cent. (JTWC), Off.  
611 U.S. Navy Website. <https://www.metoc.navy.mil/jtwc/jtwc.html?north-indian-ocean>

612 Kallepalli A, Kakani NR, James DB, Richardson MA (2017) Digital shoreline analysis system-  
613 based change detection along the highly eroding Krishna – Godavari delta front. *J Appl*  
614 *Remote Sens* 11:036018-1–11. <https://doi.org/10.1117/1.JRS.11.036018>

615 Keim B, Sathiaraj D, Brown V (2020) SURGEDAT: The World’s Storm Surge Data Center.  
616 In: *South. Clim. Impacts Plan. Progr.* <http://surge.srcc.lsu.edu/index.html>

617 Knapp KR, Kruk MC (2010) Quantifying interagency differences in tropical cyclone best-track  
618 wind speed estimates. *Mon Weather Rev* 138:1459–1473.  
619 <https://doi.org/10.1175/2009MWR3123.1>

620 Kolar RL, Gray WG, Westerink JJ, Luettich Jr. RA (1994) Shallow water modeling in spherical  
621 coordinates: equation formulation, numerical implementation, and application. *J Hydraul*  
622 *Res* 32:3–24. <https://doi.org/10.1080/00221689409498786>

623 Li A, Guan S, Mo D, et al (2020) Modeling wave effects on storm surge from different typhoon  
624 intensities and sizes in the South China Sea. *Estuar Coast Shelf Sci* 235:106551.  
625 <https://doi.org/10.1016/j.ecss.2019.106551>

626 Longuet-Higgins MS, Stewart RW (1964) Radiation stresses in water waves; a physical  
627 discussion with applications. *Deep Res Oceanogr Abstr* 11:529–562

628 Lynch DR, Gray WG (1979) A wave equation model for finite element tidal computations.  
629 *Comput Fluids* 7:207–228. [https://doi.org/10.1016/0045-7930\(79\)90037-9](https://doi.org/10.1016/0045-7930(79)90037-9)

630 McInnes KL, Walsh KJE, Hubbert GD, Beer T (2003) Impact of sea-level rise and storm surges  
631 in a coastal community. *Nat Hazards* 30:187–207.  
632 <https://doi.org/10.1023/A:1026118417752>

633 Mei W, Pasquero C, Primeau F (2012) The effect of translation speed upon the intensity of  
634 tropical cyclones over the tropical ocean. *Geophys Res Lett* 39:7.  
635 <https://doi.org/10.1029/2011GL050765>

636 Poulouse J, Rao AD, Dube SK (2020) Mapping of cyclone induced extreme water levels along

637 Gujarat and Maharashtra coasts: a climate change perspective. *Clim Dyn* 55:3565–3581.  
638 <https://doi.org/10.1007/s00382-020-05463-4>

639 Rao AD, Chittibabu P, Murty TS, et al (2007) Vulnerability from storm surges and cyclone  
640 wind fields on the coast of Andhra Pradesh, India. *Nat Hazards* 41:515–529.  
641 <https://doi.org/10.1007/s11069-006-9047-4>

642 Rao AD, Murty PLN, Jain I, et al (2013) Simulation of water levels and extent of coastal  
643 inundation due to a cyclonic storm along the east coast of India. *Nat Hazards* 66:1431–  
644 1441. <https://doi.org/10.1007/s11069-012-0193-6>

645 Rao KN, Subraelu P, Rao TV, et al (2008) Sea-level rise and coastal vulnerability : an  
646 assessment of Andhra Pradesh coast , India through remote sensing and GIS. *J Coast*  
647 *Conserv* 12:195–207. <https://doi.org/10.1007/s11852-009-0042-2>

648 Rego JL, Li C (2009) On the Receding of Storm Surge along Louisiana ’ s Low-Lying Coast.  
649 *J Coast Res SI* 56: 1045–1049. <https://www.jstor.org/stable/25737946>

650

651 Resio DT, Irish JL, Westerink JJ, Powell NJ (2013) The effect of uncertainty on estimates of  
652 hurricane surge hazards. *Nat Hazards* 66:. <https://doi.org/10.1007/s11069-012-0315-1>

653 Resio DT, Westerink JJ (2008) Modeling the physics of storm surges. *Phys Today* 9:33–38

654 Sahoo B, Bhaskaran PK (2018) A comprehensive data set for tropical cyclone storm surge-  
655 induced inundation for the east coast of India. *Int J Climatol* 38:403–419.  
656 <https://doi.org/10.1002/joc.5184>

657 Sebastian A, Proft J, Dietrich JC, et al (2014) Characterizing hurricane storm surge behavior  
658 in Galveston Bay using the SWAN+ADCIRC model. *Coast Eng* 88:171–181.  
659 <https://doi.org/10.1016/j.coastaleng.2014.03.002>

660 Sebastian M, Behera MR (2015) Impact of SST on tropical cyclones in North Indian Ocean.  
661 In: *Procedia Engineering*. Elsevier B.V., pp 1072–1077.  
662 <https://doi.org/10.1016/j.proeng.2015.08.346>

663 Sebastian M, Behera MR (2018) Surge Height and Current Estimation Along K-G Basin. In:  
664 *Proceedings of the International Conference on Offshore Mechanics and Arctic*  
665 *Engineering - OMAE*. American Society of Mechanical Engineers, Madrid, Spain., pp 1–

666 9. <https://doi.org/10.1115/OMAE2018-77945>

667 Sebastian M, Behera MR, Murty PLN (2019) Storm surge hydrodynamics at a concave coast  
668 due to varying approach angles of cyclone. *Ocean Eng* 191:1–16.  
669 <https://doi.org/10.1016/j.oceaneng.2019.106437>

670 Sindhu B, Unnikrishnan AS (2012) Return period estimates of extreme sea level along the east  
671 coast of India from numerical simulations. *Nat Hazards* 61:1007–1028.  
672 <https://doi.org/10.1007/s11069-011-9948-8>

673 Singh VK, Roxy MK (2020) A review of the ocean-atmosphere interactions during tropical  
674 cyclones in the north Indian Ocean. *arXiv preprint arXiv:2012.04384*

675 Thomas A, Dietrich JC, Asher TG, et al (2019) Influence of storm timing and forward speed  
676 on tides and storm surge during Hurricane Matthew. *Ocean Model* 137:1–19.  
677 <https://doi.org/10.1016/j.ocemod.2019.03.004>

678 Willoughby HE, Rahn ME (2004) Parametric Representation of the Primary Hurricane Vortex  
679 . Part I: Observations and evaluation of the Holland (1980) model. *Mon Weather Rev*  
680 132:3033–3048. <https://doi.org/10.1175/MWR2831.1>

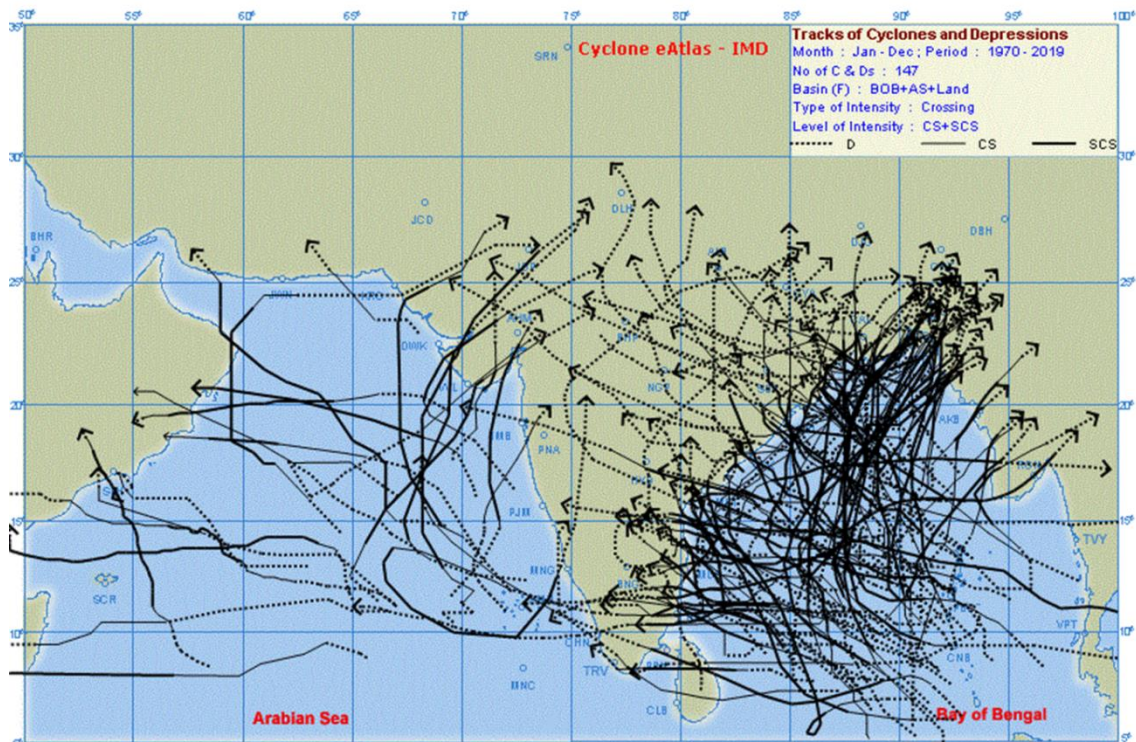
681 Wu L, Wen Z, Huang R (2020) Tropical cyclones in a warming climate. *Sci China Earth Sci*.  
682 <https://doi.org/10.1007/s11430-019-9574-4>

683 Zijlema M (2010) Computation of wind-wave spectra in coastal waters with SWAN on  
684 unstructured grids. *Coast Eng* 57:267–277.  
685 <https://doi.org/10.1016/j.coastaleng.2009.10.011>

686

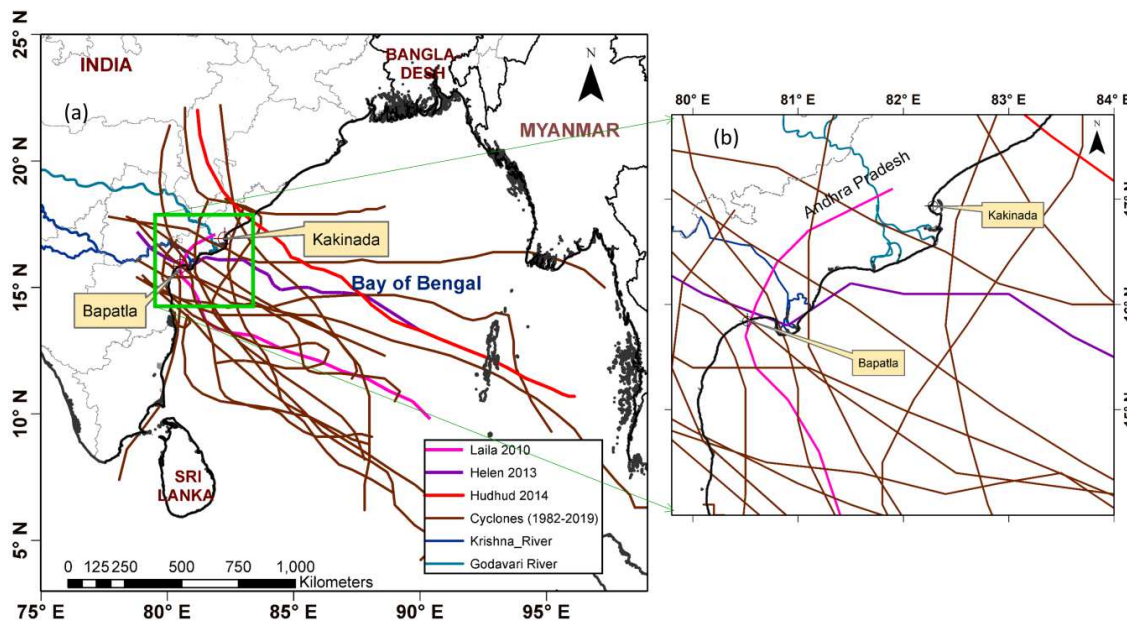
687

688 **Figure Captions**

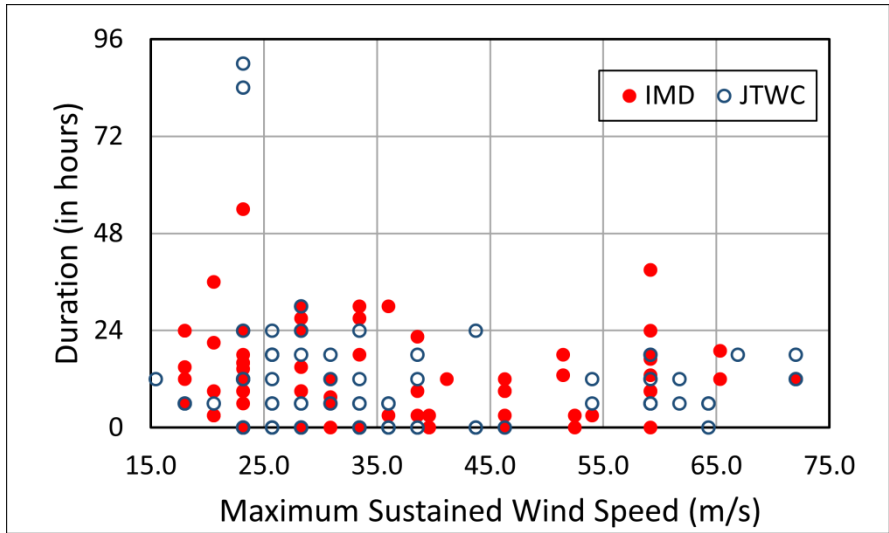


689  
690 Figure 1 Cumulative tracks of landfalling TCs in NIO region from 1970-2019 (Source : Cyclone eAtlas-IMD  
691 2020)

692

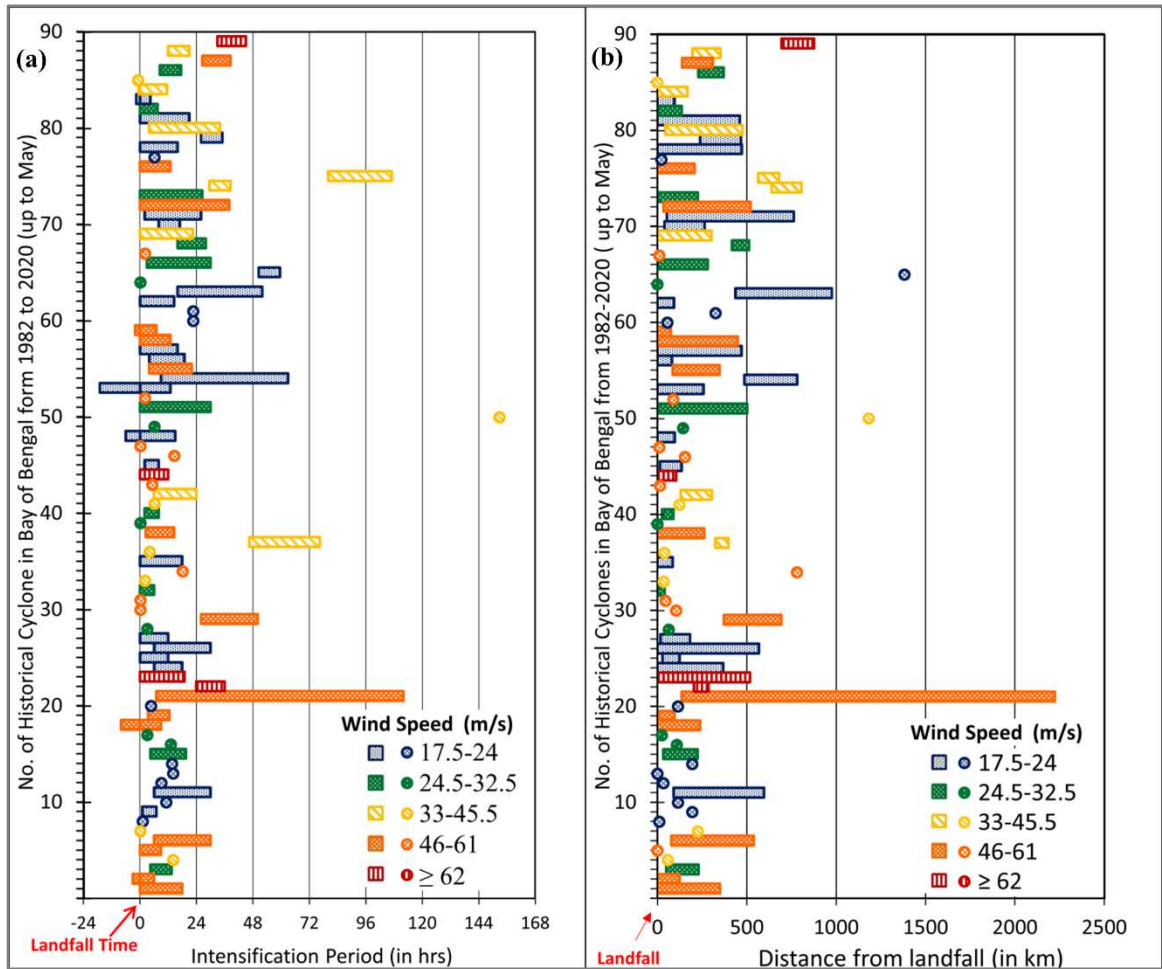


693  
694 Figure 2(a) Cyclone tracks from year 1982-2019 landfalling in Andhra Pradesh Coast, and(b) Enlarged view  
695 along the coast of K-G Basin



696  
697  
698

Figure 3 Scatterplot representing the highest associated cyclone intensity and its duration from IMD and JTWC for cyclones landfalling in BoB from 1982-2018

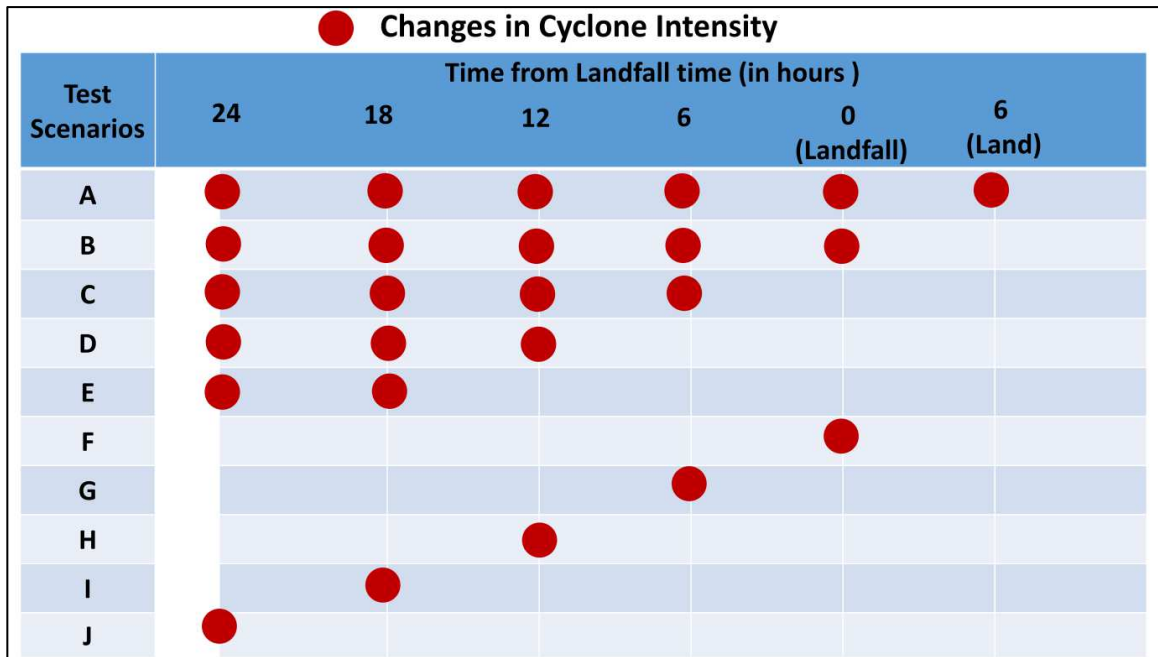


699

700  
701  
702

Figure 4 Landfalling TCs in BoB from 1982-2020 (up to May) with their highest maximum sustained wind speed and (a) duration by highest wind speed with respect to landfall time (represented by 0 in the X axis) (b) distance travelled by highest wind speed estimated from the landfall location (represented by 0 in the X axis)

703

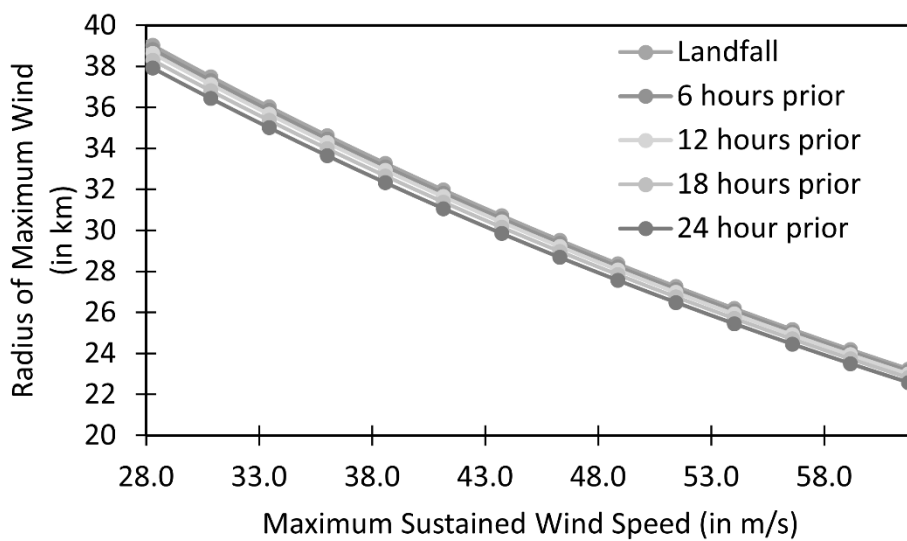


704

705

706

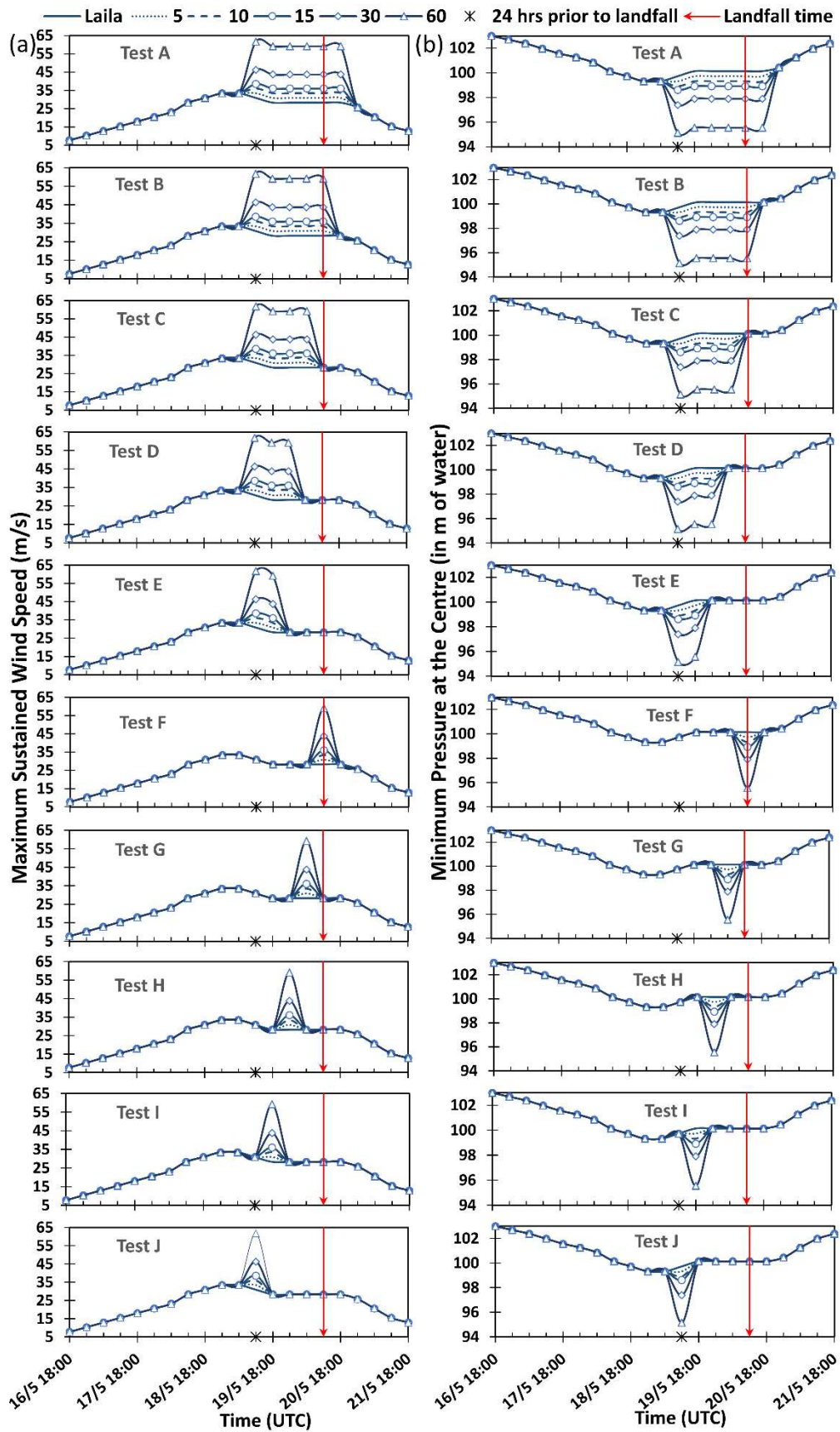
Figure 5 Hypothetical test scenarios showing the cyclone path on temporal scale 24 hours prior to landfall and 6 hours after landfall where the cyclone intensities are altered



707

708

Figure 6 Radius of Maximum Winds corresponding to Maximum Sustained Wind Speed



709

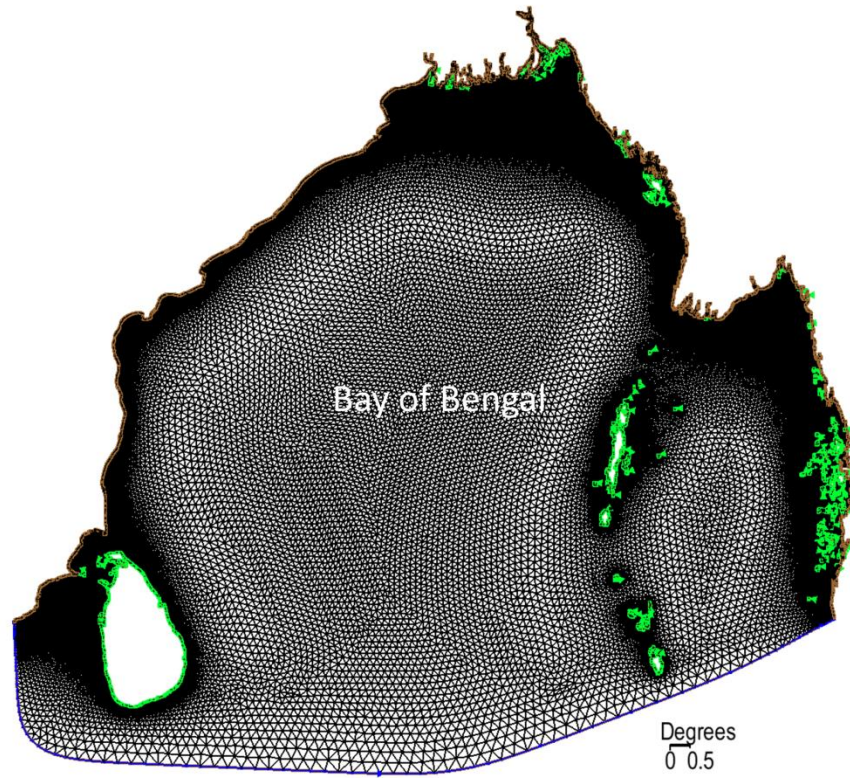
710

711

712

Figure 7 Temporal Variation of (a) Maximum sustained wind intensity of *Laila* and increased by 2.57(5), 5.14(10), 7.71(15), 15.4 (15) and 30.86 (60) m/s (knots) for different durations (A to J), and (b) Central Pressure for *Laila* and the corresponding changes in the pressure for different durations (A to J) considered for the study

713

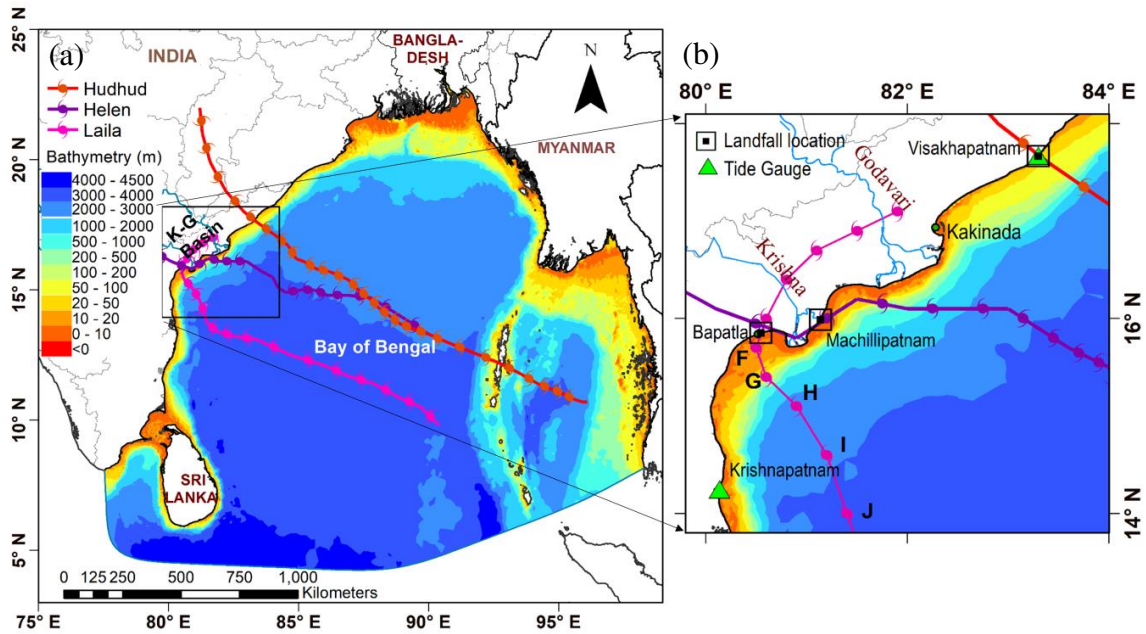


714

715

Figure 8 Discretised BoB Domain

716



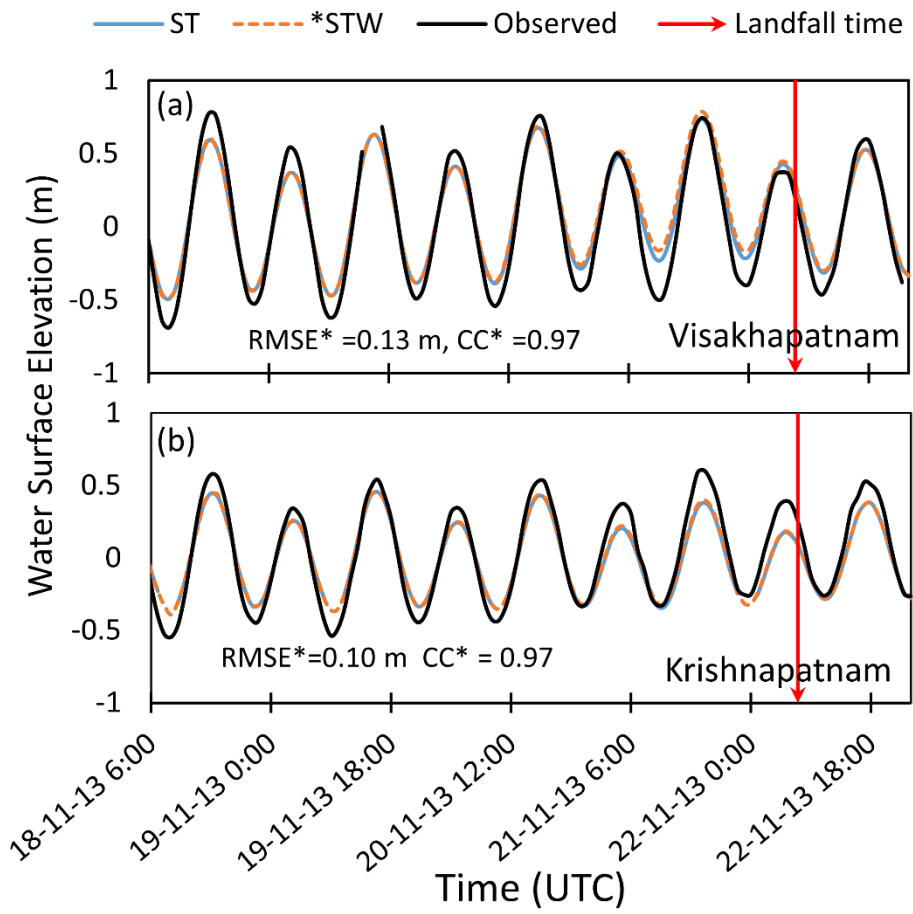
717

718

719

720

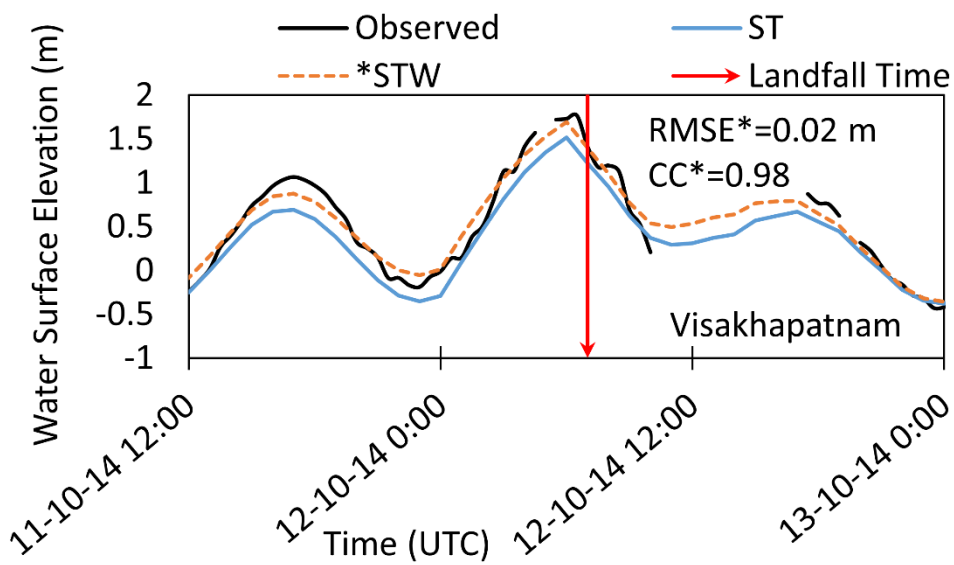
Figure 9(a) Study domain with interpolated bathymetry and the tracks of *Laila*, *Helen*, and *Hudhud* cyclones, and (b) Enlarged View showing the tide gauge stations and location along the *Laila* track where the intensities are varied for the present study



721

722  
723

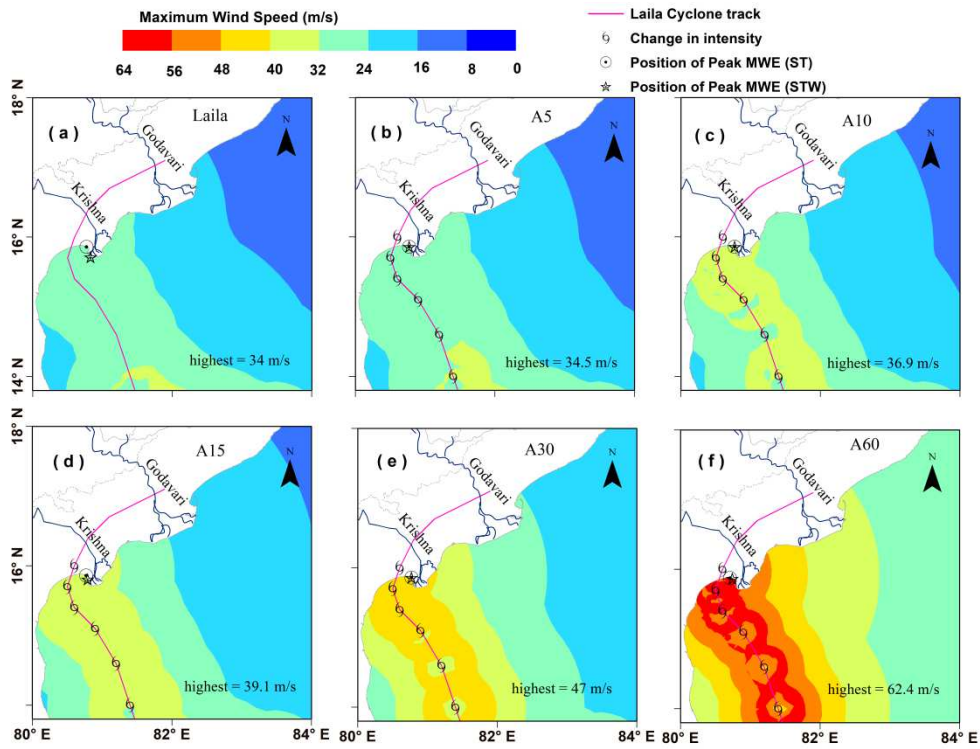
Figure 10 Comparison of observed and computed Water Levels at Visakhapatnam and Krishnapatnam during Helen 2013



724

725  
726

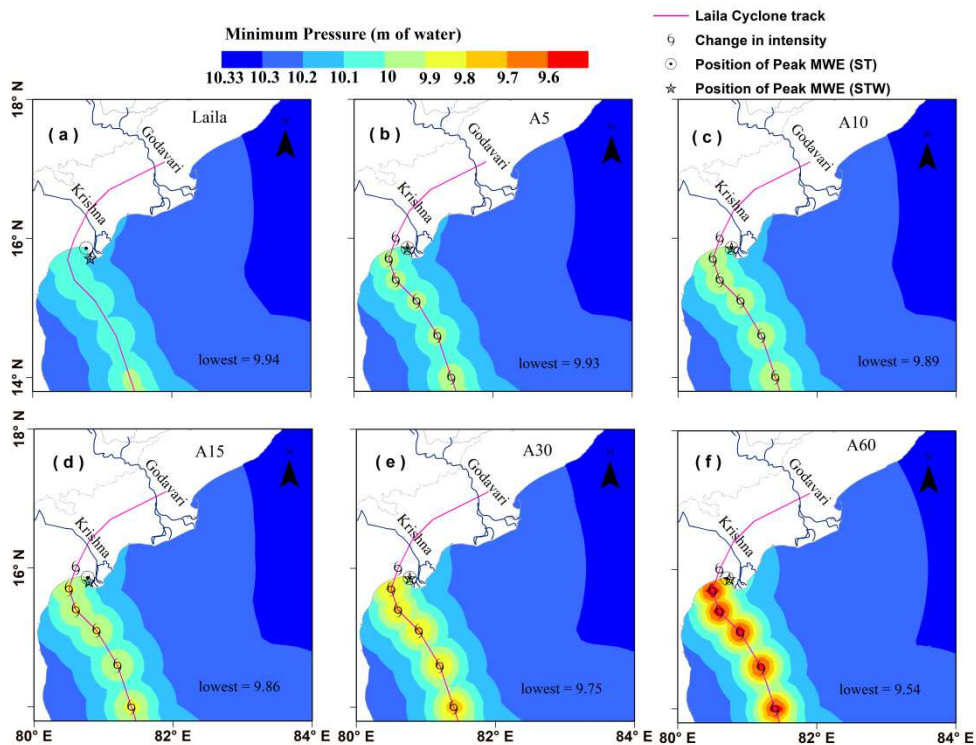
Figure 11 Comparison of observed and computed Water Levels at Visakhapatnam during an ESCS Hudhud 2014



727

728  
729  
730

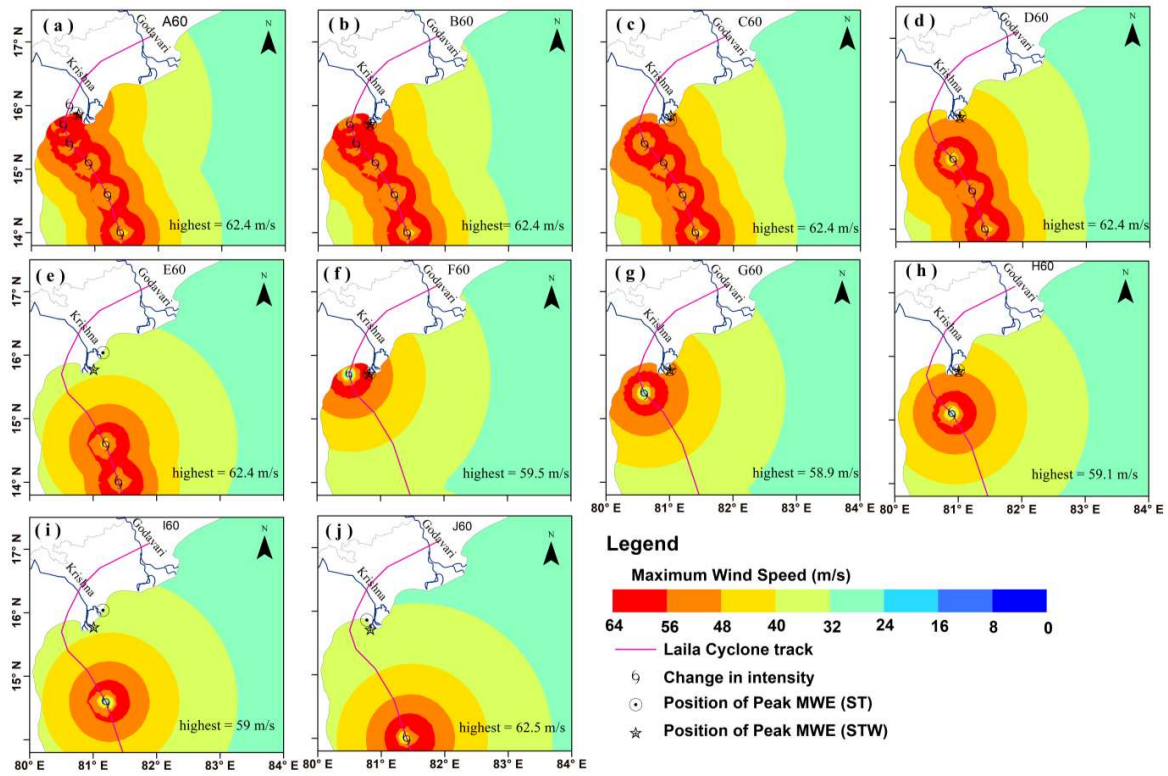
Figure 12 Spatial plot of Maximum Wind Speed during (a) *Laila* Cyclone and for Test A Scenario where the wind speed increased by (b) 2.57 m/s (5 knots), (c) 5.14 m/s (10 knots), (d) 7.71 m/s (15 knots), (e) 15.4 m/s (30 knots), and (f) 30.86 m/s (60 knots)



731

732  
733  
734

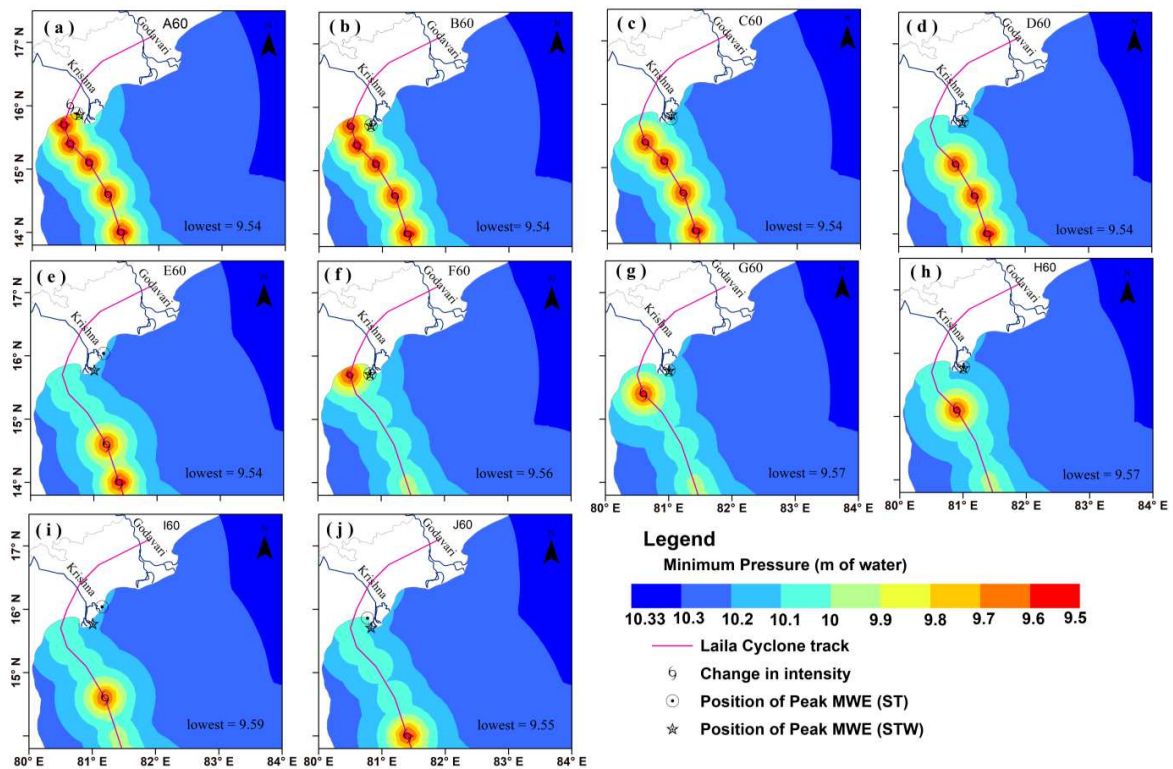
Figure 13 Spatial extent of Minimum Pressure during (a) *Laila* Cyclone, and for Test Scenario A where the wind speed increased by (b) 2.57 m/s (5 knots), (c) 5.14 m/s (10 knots), (d) 7.71 m/s (15 knots), (e) 15.4 m/s (30 knots), and (f) 30.86 m/s (60 knots)



735

736  
737

Figure 14 Spatial plot of Maximum Wind Speed with 30 m/s (60 knots) increase for different test scenarios (A - J)



738  
739  
740

Figure 15 Spatial extent of Minimum Pressure for different Test Scenarios with an increasing wind speed by 30.86 m/s (60 knots) considered for the study

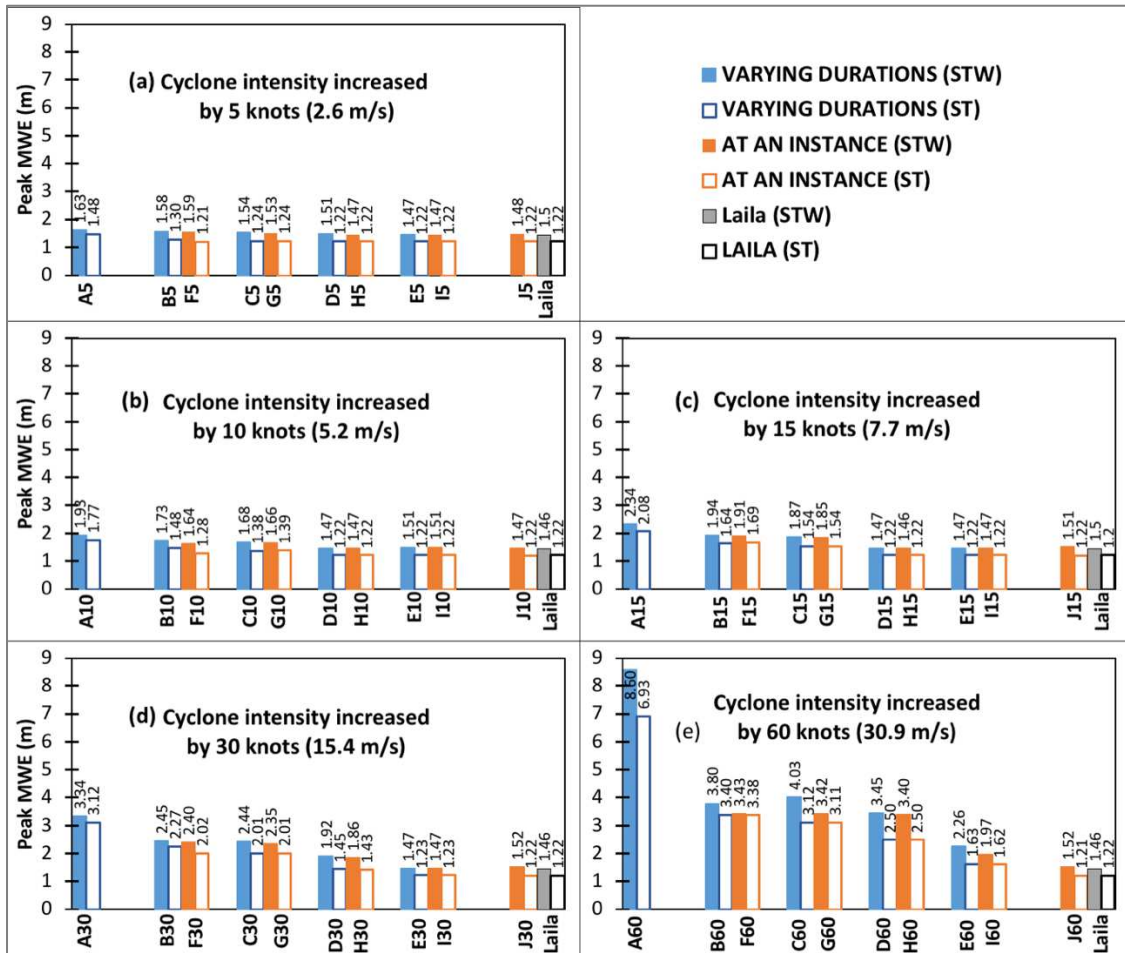


Figure 16 Peak Maximum Water Levels recorded by ST and STW along the K-G basin of *Laila* along with those of cyclone intensities increase by (a) 2.57 m/s (5 knots), (b) 5.14 m/s (10 knots), (c) 7.71 m/s (15 knots), (d) 15.4 m/s (30 knots), and (e) 30.86 m/s (60 knots) for 10 test scenarios

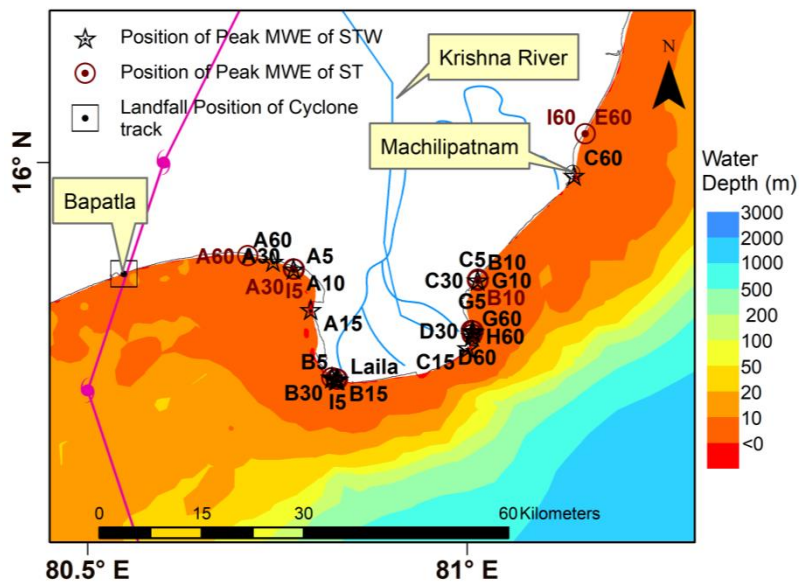
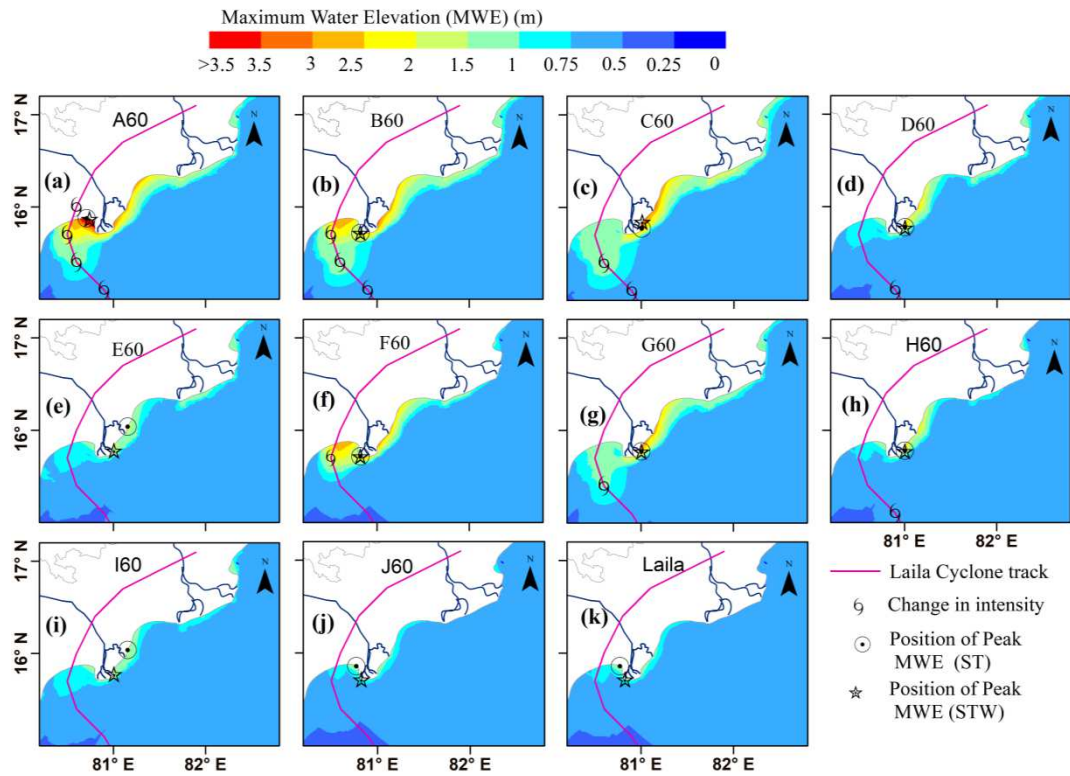


Figure 17 Location showing the Peak MWEs of STW and ST

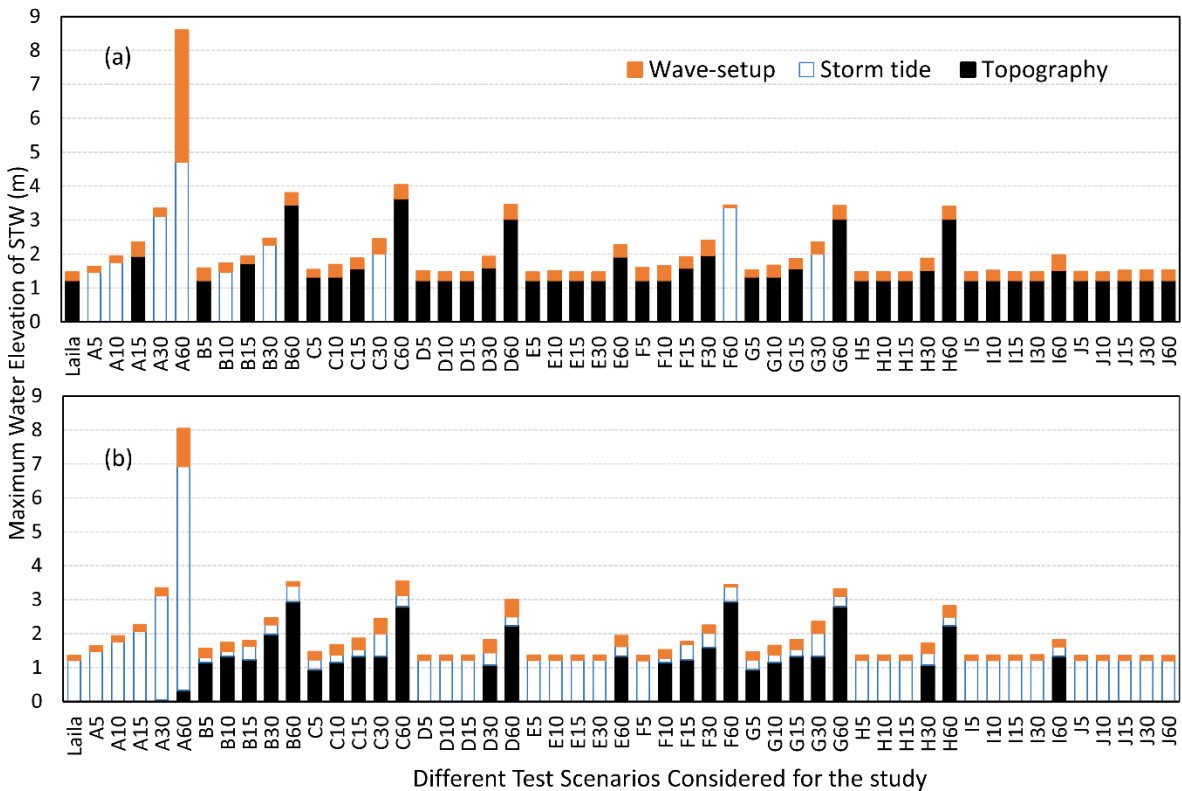
741  
742  
743  
744

745  
746



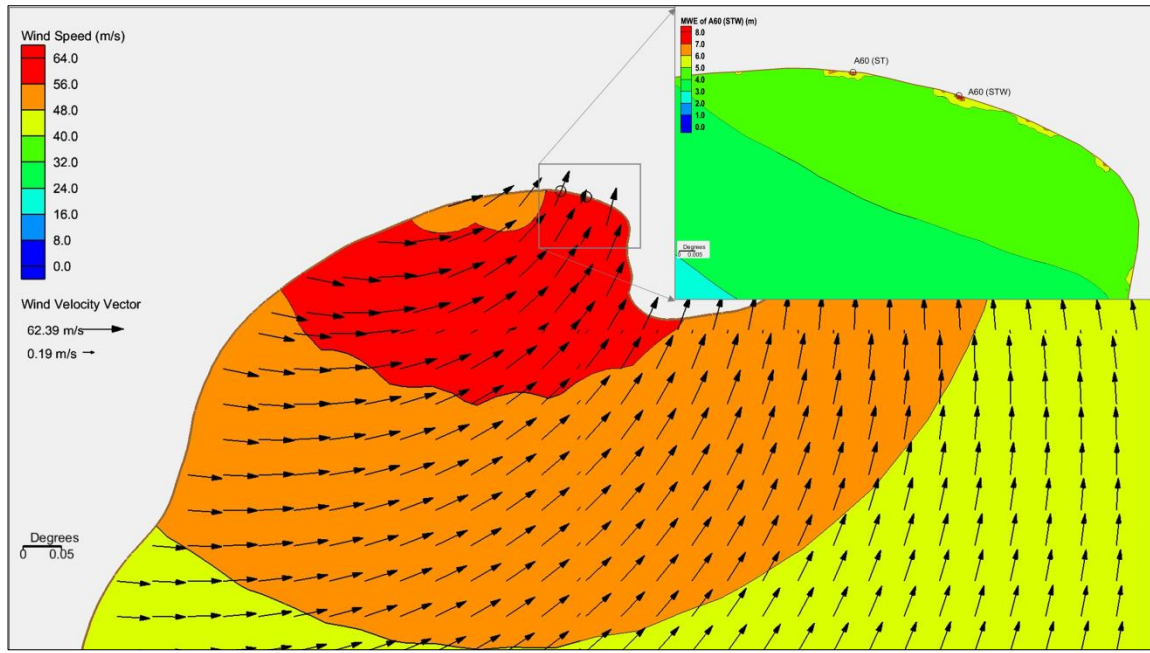
747  
748  
749

Figure 18 Spatial plot showing MWE of STW along the K-G basin for cyclone with increasing wind speed by 30.86 m/s (60 knots) for different durations(a-j), and (k) Laila



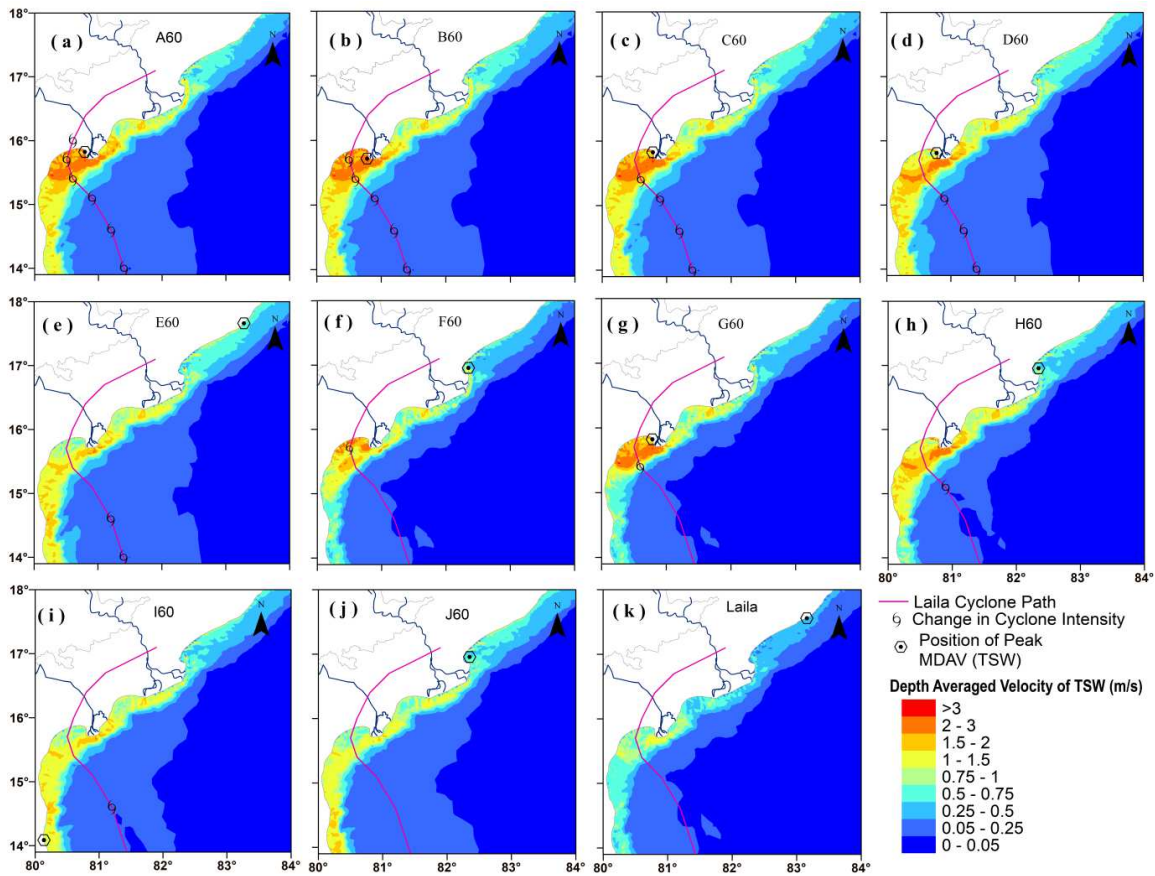
750  
751  
752

Figure 19 Wave contributions of all the numerical simulations at (a) location of peak MWE of STW (b) location of peak MWE of ST



753  
754  
755

Figure 20 Wind field of Test A60 during the peak MWE for STW and the enlarged MWE showing the peak MWE (top right corner)



756  
757  
758

Figure 21 Spatial extent of  $V_{avg\_max}$  with increasing wind speed by 30.86 m/s (60 knots) for different durations considered for the study

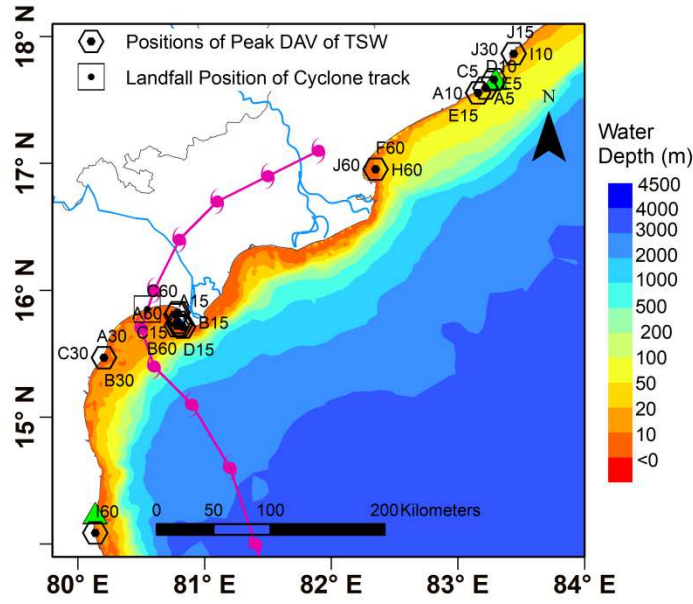


Figure 22 Locations of peak  $V_{avg\_max}$  for all the scenarios

759  
760

761 **Table Captions**

762 Table 1 IMD classification of low-pressure system over the Indian Ocean

T-Number/ C.I. Number	System	Maximum Sustained Wind Speed (m/s)	Pressure Drop (hPa)
T1.5	Depression (D)	8-14	1.0- 3.0
T2.0	Deep Depression (DD)	14.5–17	3.0 - 4.5
T2.5	Cyclonic Storm (CS)	17.5 -24	6.1- 10
T3.5	Severe Cyclonic Storm (SCS)	24.5-32.5	15
T4.0	Very Severe Cyclonic Storm (VSCS)	33-45.5	20.9-29.4
T5.0	Extremely Severe Cyclonic Storm (ESCS)	46-61	40.2-65.6
T6.5	Super Cyclonic Storm (SuCS)	$\geq 62$	$\geq 80$

763

764 Table 2 Details of the numerical simulations conducted

Model	Increased Maximum sustained wind speed m/s (knots)	Intensification durations	Experiments
ADCIRC	2.57(5), 5.14 (10), 7.71 (15), 15.4 (30) &30.86 (60)	A, B, C,D, E,F,G, H, I, J	5x10=50 + Laila
ADCIRC+SWAN	2.57(5), 5.14 (10), 7.71 (15), 15.4 (30) &30.86 (60)	A, B, C,D, E,F,G, H, I, J	5x10=50 + Laila
Total Experiments			102

765

766

767  
768  
769  
770

771  
772  
773

Table 3 Highest of the Maximum Wind Speeds (m/s) & Lowest of the Minimum Central Pressures (m of water) for all the considered test cases

Test Scenarios	2.57 m/s (5 knots)		5.14m/s (10 knots)		7.71 m/s(15 knots)		15.4 m/s (30 knots)		30.86 m/s (60 knots)	
	Wind Speed	Central Pressure	Wind Speed	Central Pressure	Wind Speed	Central Pressure	Wind Speed	Central Pressure	Wind Speed	Central Pressure
A	34.5	9.93	36.9	9.89	39.1	9.86	47	9.75	62.4	9.54
B	34.5	9.93	36.9	9.89	39.1	9.86	47	9.75	62.4	9.54
C	34.5	9.93	36.9	9.89	39.1	9.86	47	9.75	62.4	9.54
D	34.5	9.93	36.9	9.89	39.1	9.86	47	9.75	62.4	9.54
E	34.5	9.93	36.9	9.89	39.1	9.86	47	9.75	62.4	9.54
F	34	9.94	34.1	9.93	36.8	9.89	44.6	9.79	59.5	9.56
G	34	9.94	34.1	9.93	36.7	9.89	44.2	9.79	58.9	9.57
H	34	9.94	34.3	9.93	36.7	9.89	44.1	9.79	59.1	9.57
I	34	9.94	34.5	9.94	37	9.90	44.4	9.80	59.0	9.59
J	34.5	9.93	36.9	9.89	39.2	9.87	47.1	9.75	62.5	9.55

774  
775  
776  
777

Table 4 Percentage change in the peak MWE(STW) for all the test cases with respect to the peak MWE of *Laila* (STW)

Test Scenarios	2.57 m/s (5 knots)	5.14 m/s (10 knots)	7.71 ms/ (15 knots)	15.4 m/s (30 knots)	30.86 m/s (60 knots)
A	11.5	32.0	60.1	128.3	487.4
B	8.1	18.3	32.2	67.7	159.7
C	4.9	15.1	28.0	66.7	175.5
D	2.8	0.6	0.6	31.2	135.5
E	0.2	2.9	0.6	0.1	54.5
F	8.4	12.1	30.5	64.3	134.5
G	4.4	13.4	26.7	60.6	133.5
H	0.6	0.6	-0.1	27.2	132.0
I	0.5	3.0	0.3	0.3	34.5
J	1.1	0.2	3.4	3.6	3.6

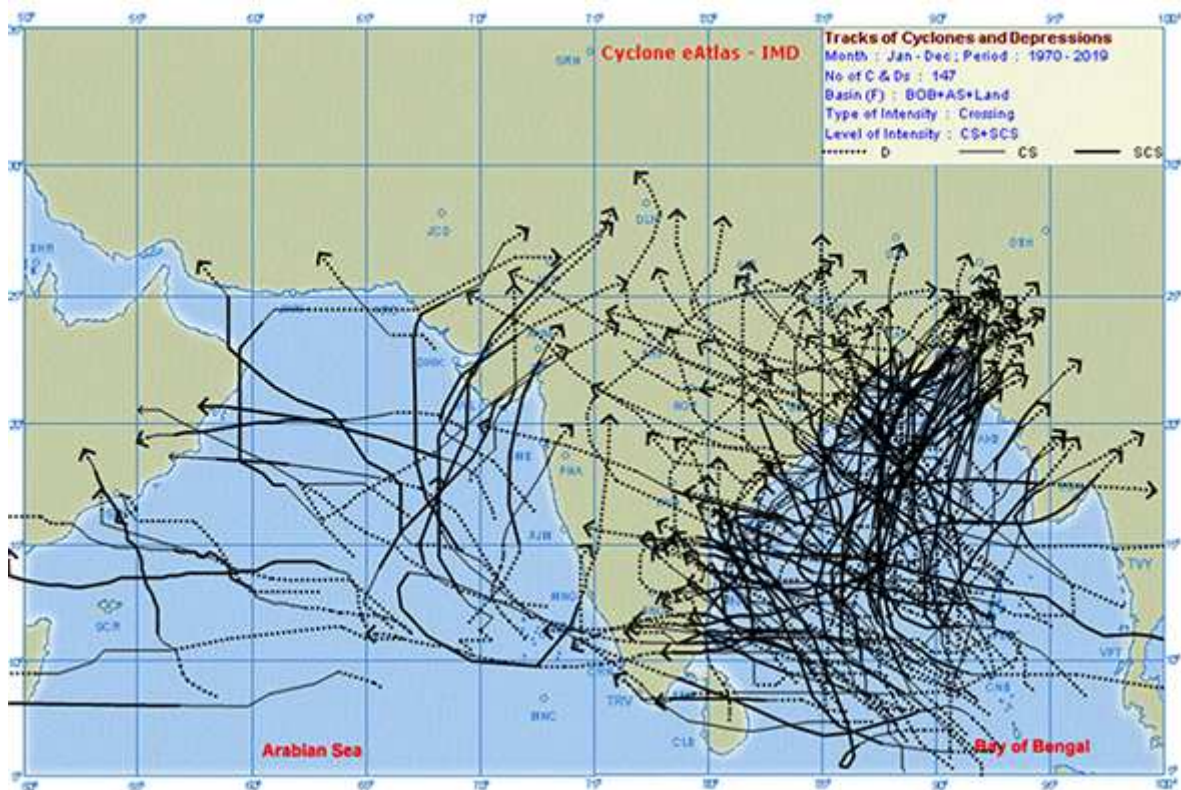
778

Table 5 Peak  $V_{avg\_max}$  (in m/s) for different scenarios and intensifications

Test Scenarios	2.57 m/s (5 knots)	5.14 m/s (10 knots)	7.71 m/s (15 knots)	15.4 m/s (30 knots)	30.86 m/s (60 knots)
A	5.2	5.1	6.3	7.9	10.3
B	5.2	5.1	6.0	7.9	10.1
C	5.2	5.5	6.0	8.5	12.2
D	5.2	4.9	6.0	6.4	10.6
E	5.6	5.6	5.3	5.5	6.1
F	5.4	5.4	5.4	5.4	6.1
G	5.0	5.0	5.0	5.6	10.4
H	5.3	5.6	5.9	6.4	7.9
I	4.9	5.6	5.5	5.5	7.8
J	5.3	5.2	5.3	6.0	7.9

779

# Figures



**Figure 1**

Cumulative tracks of landfalling TCs in NIO region from 1970-2019 (Source : Cyclone eAtlas-IMD 2020)

Note: The designations employed and the presentation of the material on this map do not imply the expression of any opinion whatsoever on the part of Research Square concerning the legal status of any country, territory, city or area or of its authorities, or concerning the delimitation of its frontiers or boundaries. This map has been provided by the authors.

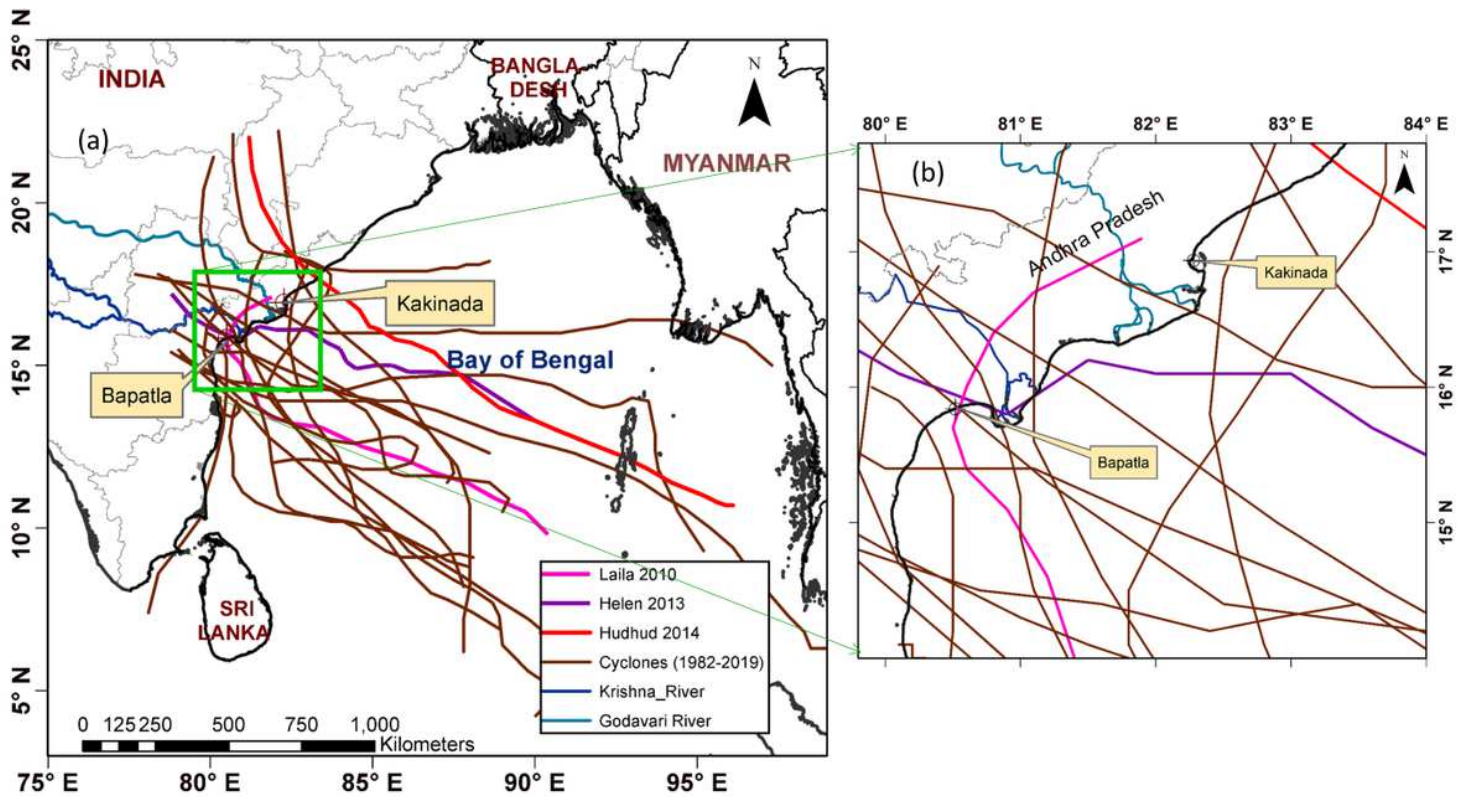


**Figure 2**

(a) Cyclone tracks from year 1982-2019 landfalling in Andhra Pradesh Coast, and (b) Enlarged view along the coast of K-G Basin. Note: The designations employed and the presentation of the material on this map do not imply the expression of any opinion whatsoever on the part of Research Square concerning the legal status of any country, territory, city or area or of its authorities, or concerning the delimitation of its frontiers or boundaries. This map has been provided by the authors.

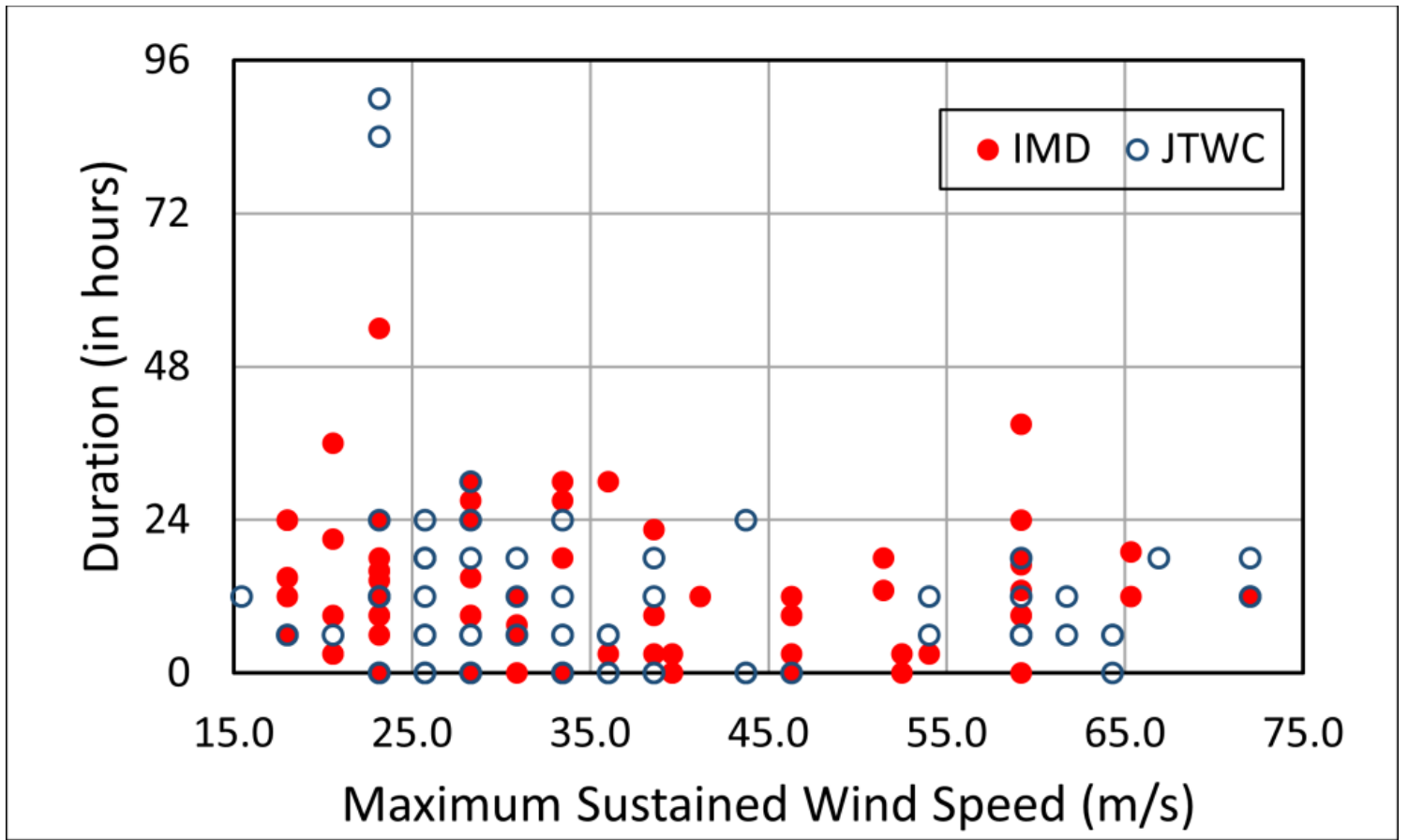
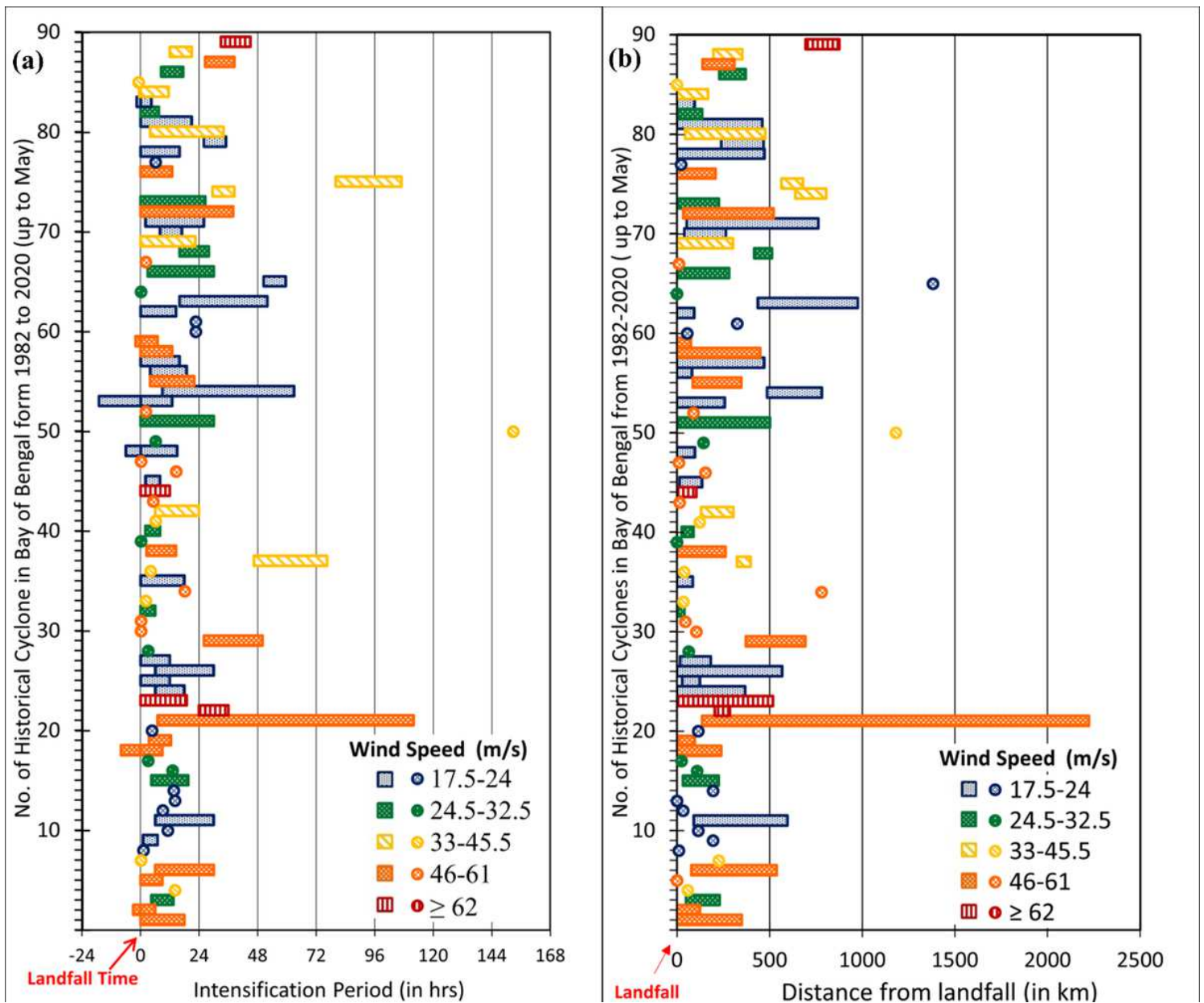


Figure 3

Scatterplot representing the highest associated cyclone intensity and its duration from IMD and JTWC for cyclones landfalling in BoB from 1982-2018



**Figure 4**

Landfalling TCs in BoB from 1982-2020 (up to May) with their highest maximum sustained wind speed and (a) duration by highest wind speed with respect to landfall time (represented by 0 in the X axis) (b) distance travelled by highest wind speed estimated from the landfall location (represented by 0 in the X axis)

**● Changes in Cyclone Intensity**

Test Scenarios	Time from Landfall time (in hours )					
	24	18	12	6	0 (Landfall)	6 (Land)
A	●	●	●	●	●	●
B	●	●	●	●	●	
C	●	●	●	●		
D	●	●	●			
E	●	●				
F					●	
G				●		
H			●			
I		●				
J	●					

**Figure 5**

Hypothetical test scenarios showing the cyclone path on temporal scale 24 hours prior to landfall and 6 hours after landfall where the cyclone intensities are altered

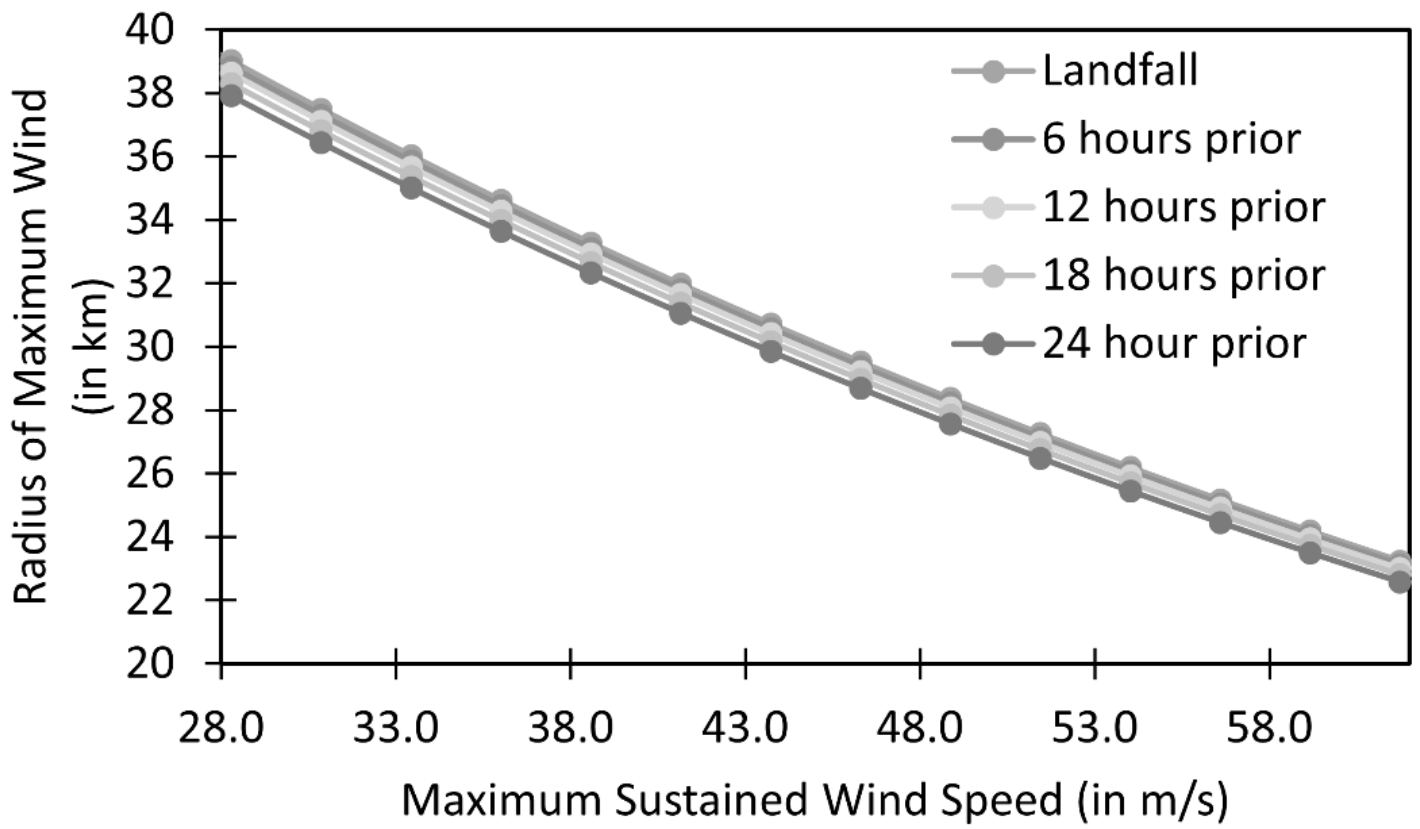
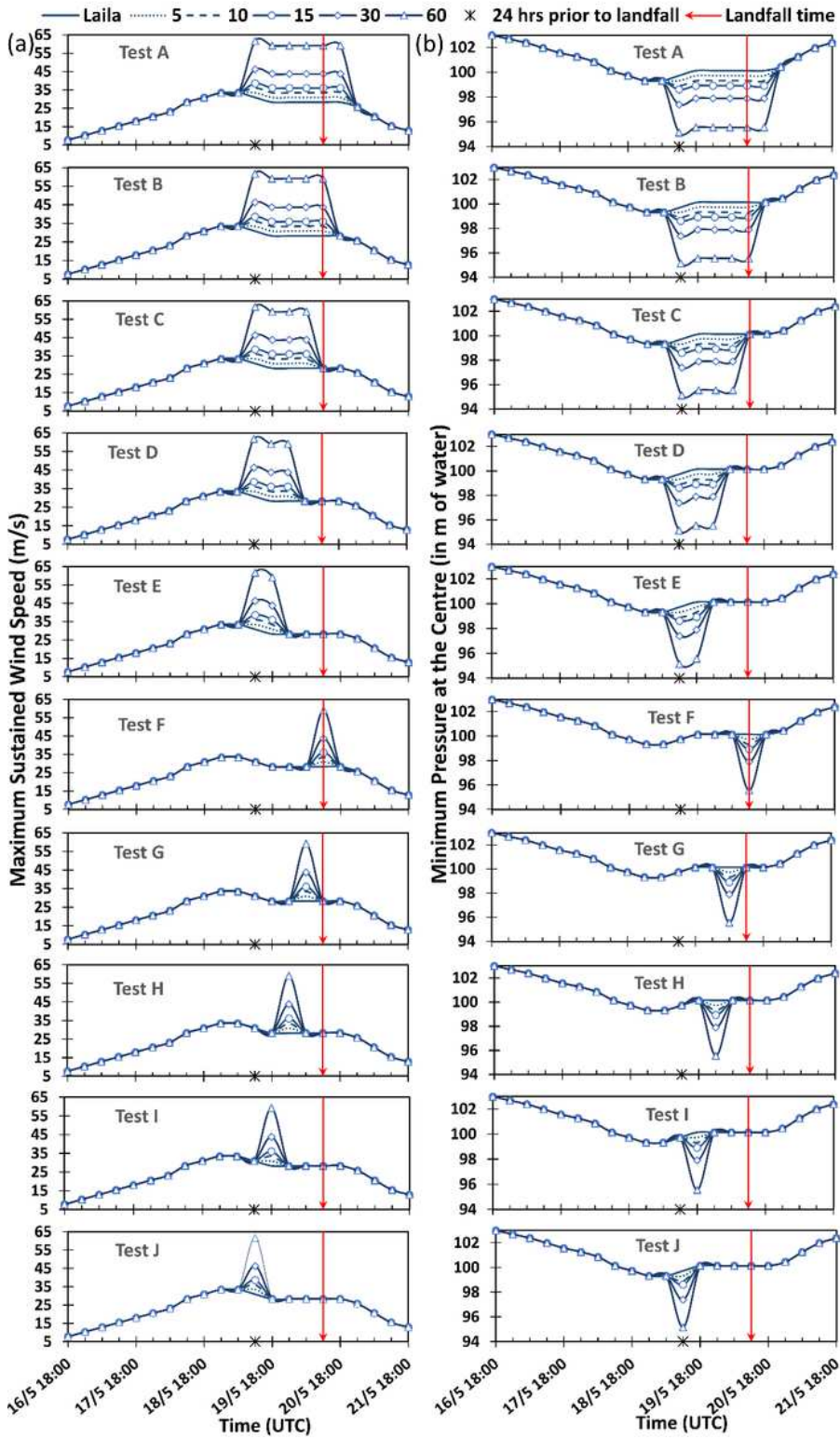


Figure 6

Radius of Maximum Winds corresponding to Maximum Sustained Wind Speed



**Figure 7**

Temporal Variation of (a) Maximum sustained wind intensity of Laila and increased by 2.57(5), 5.14(10), 7.71(15), 15.4 (15) and 30.86 (60) m/s (knots) for different durations (A to J), and (b) Central Pressure for Laila and the corresponding changes in the pressure for different durations (A to J) considered for the study

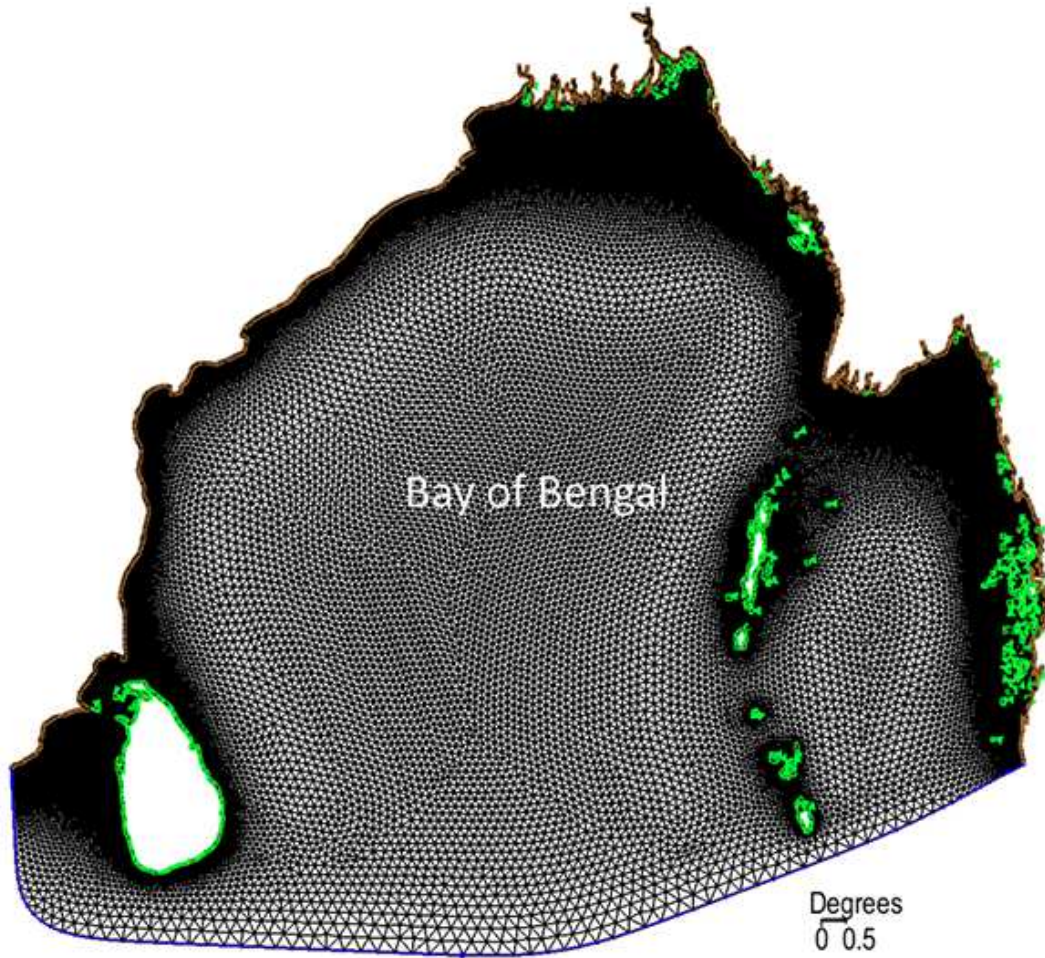


**Figure 8**

Discretised BoB Domain. Note: The designations employed and the presentation of the material on this map do not imply the expression of any opinion whatsoever on the part of Research Square concerning the legal status of any country, territory, city or area or of its authorities, or concerning the delimitation of its frontiers or boundaries. This map has been provided by the authors.

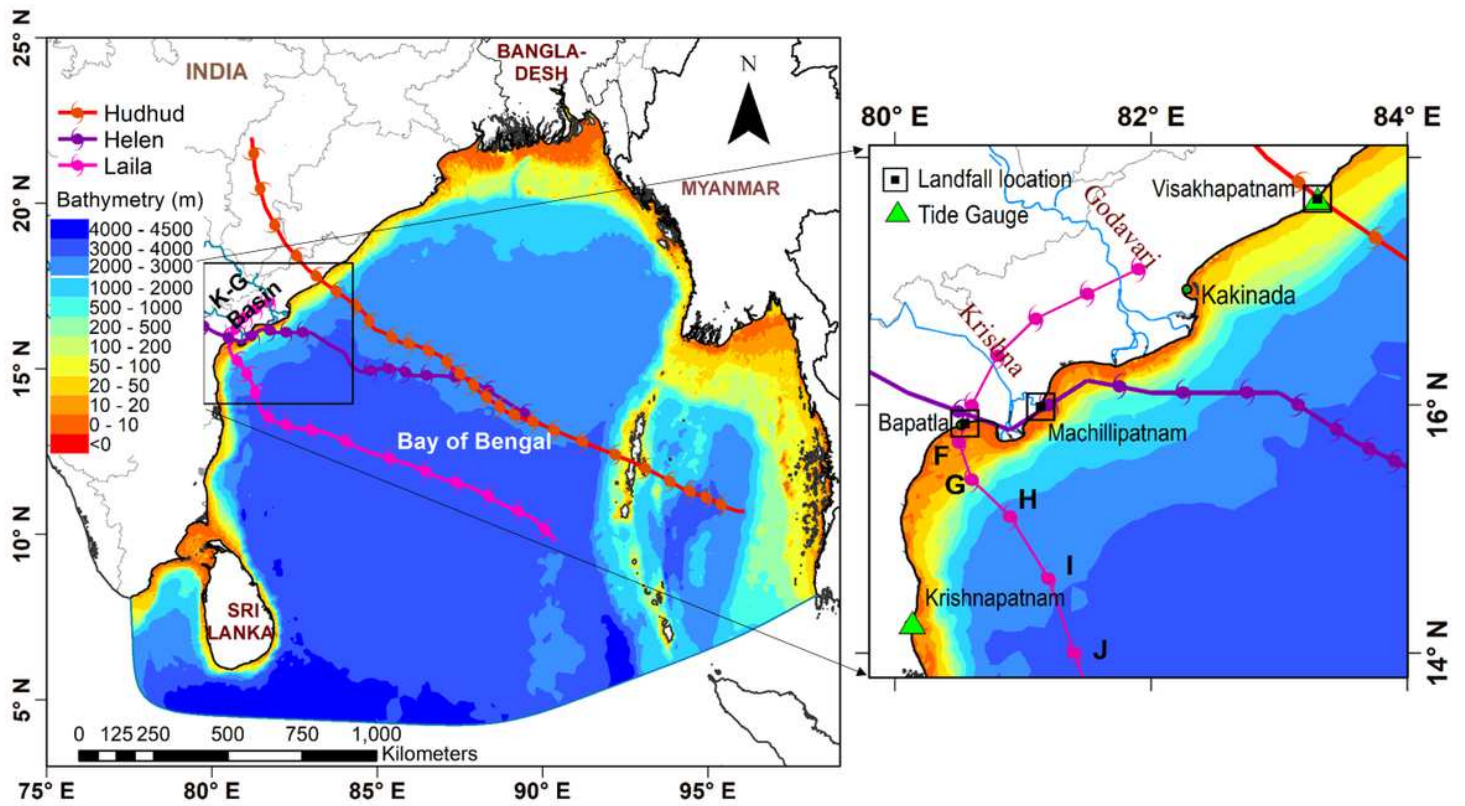


**Figure 9**

(a) Study domain with interpolated bathymetry and the tracks of Laila, Helen, and Hudhud cyclones, and (b) Enlarged View showing the tide gauge stations and location along the Laila track where the intensities are varied for the present study Note: The designations employed and the presentation of the material on this map do not imply the expression of any opinion whatsoever on the part of Research Square concerning the legal status of any country, territory, city or area or of its authorities, or concerning the delimitation of its frontiers or boundaries. This map has been provided by the authors.

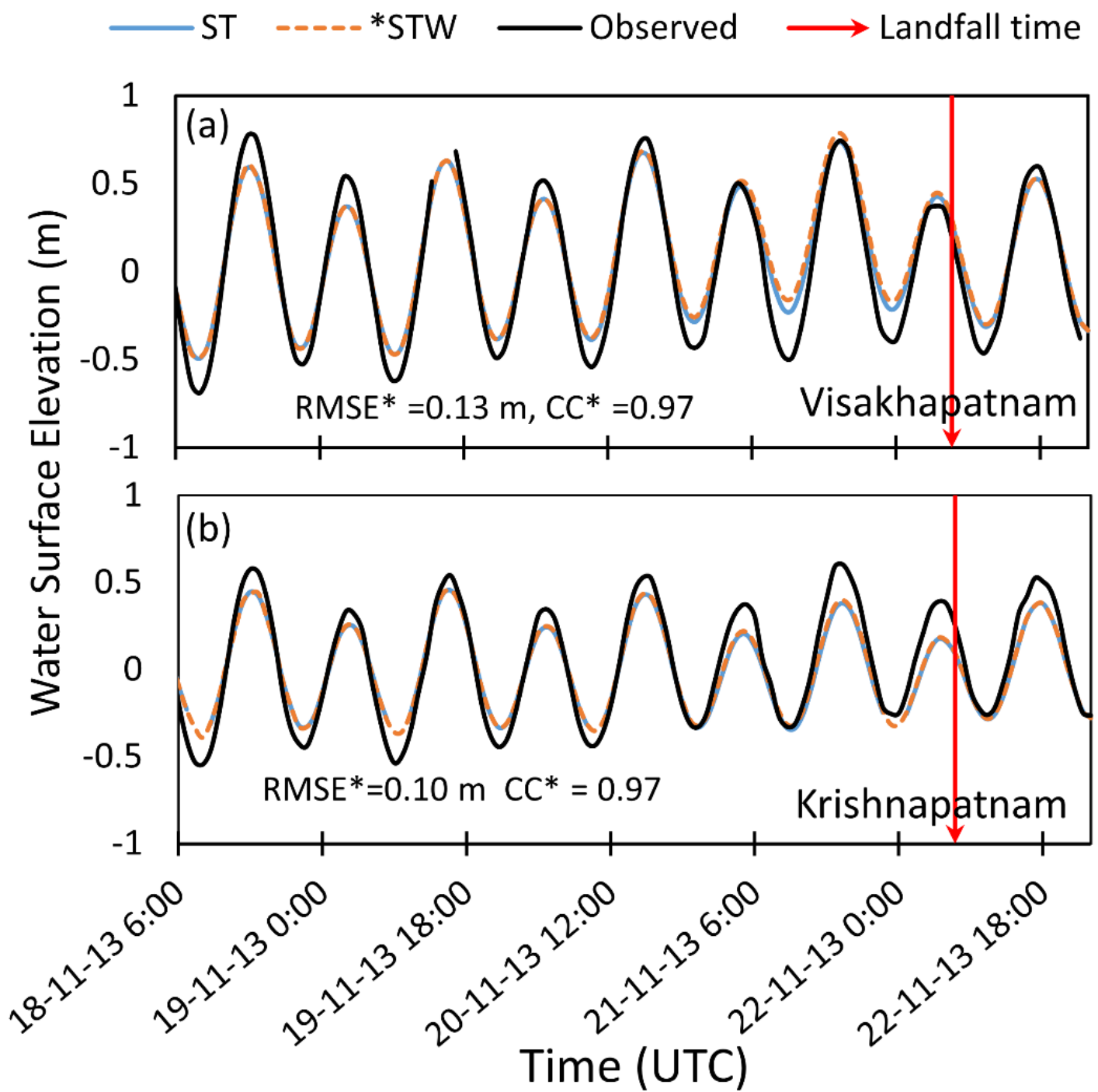


Figure 10

Comparison of observed and computed Water Levels at Visakhapatnam and Krishnapatnam during Helen 2013

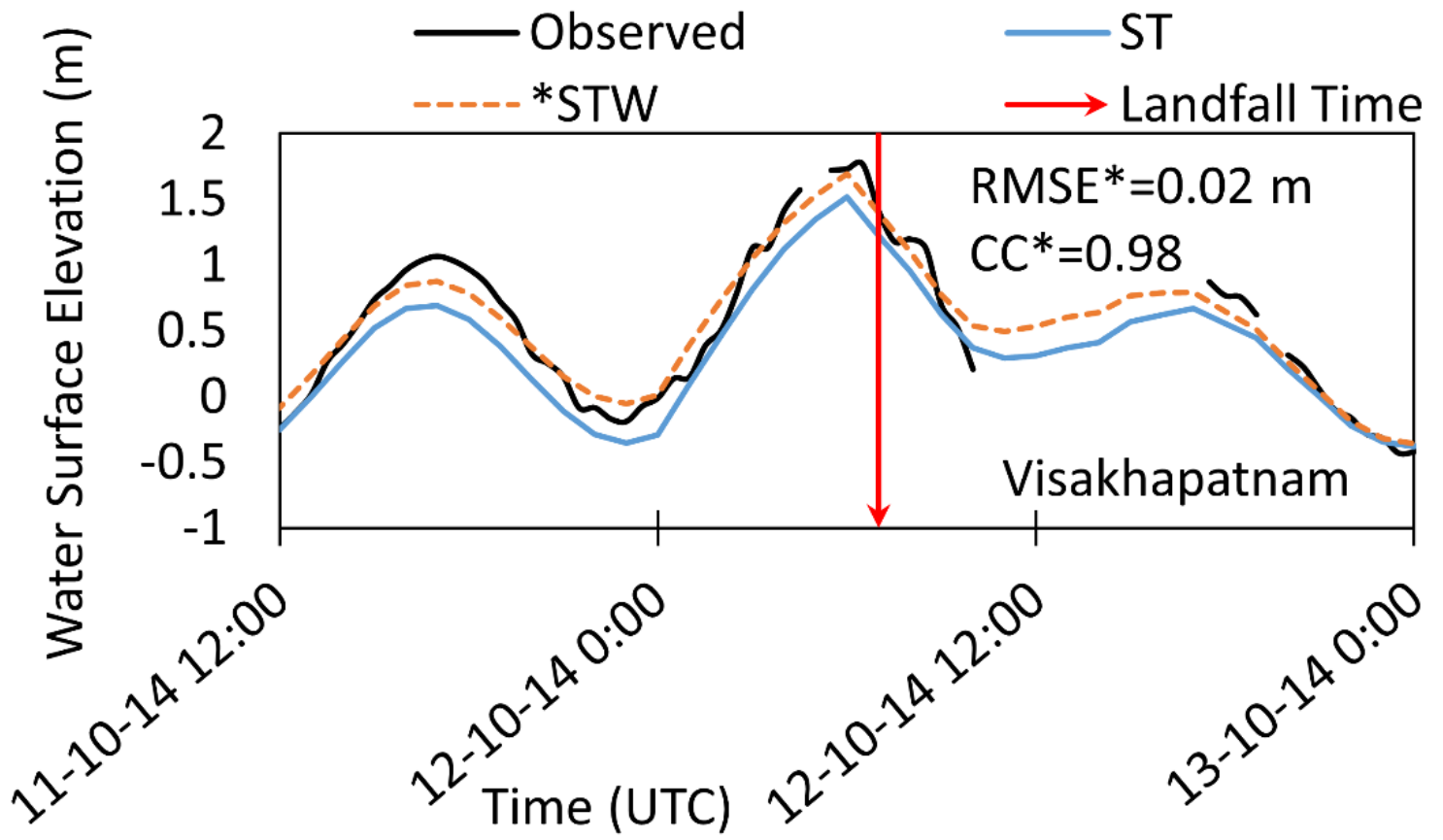
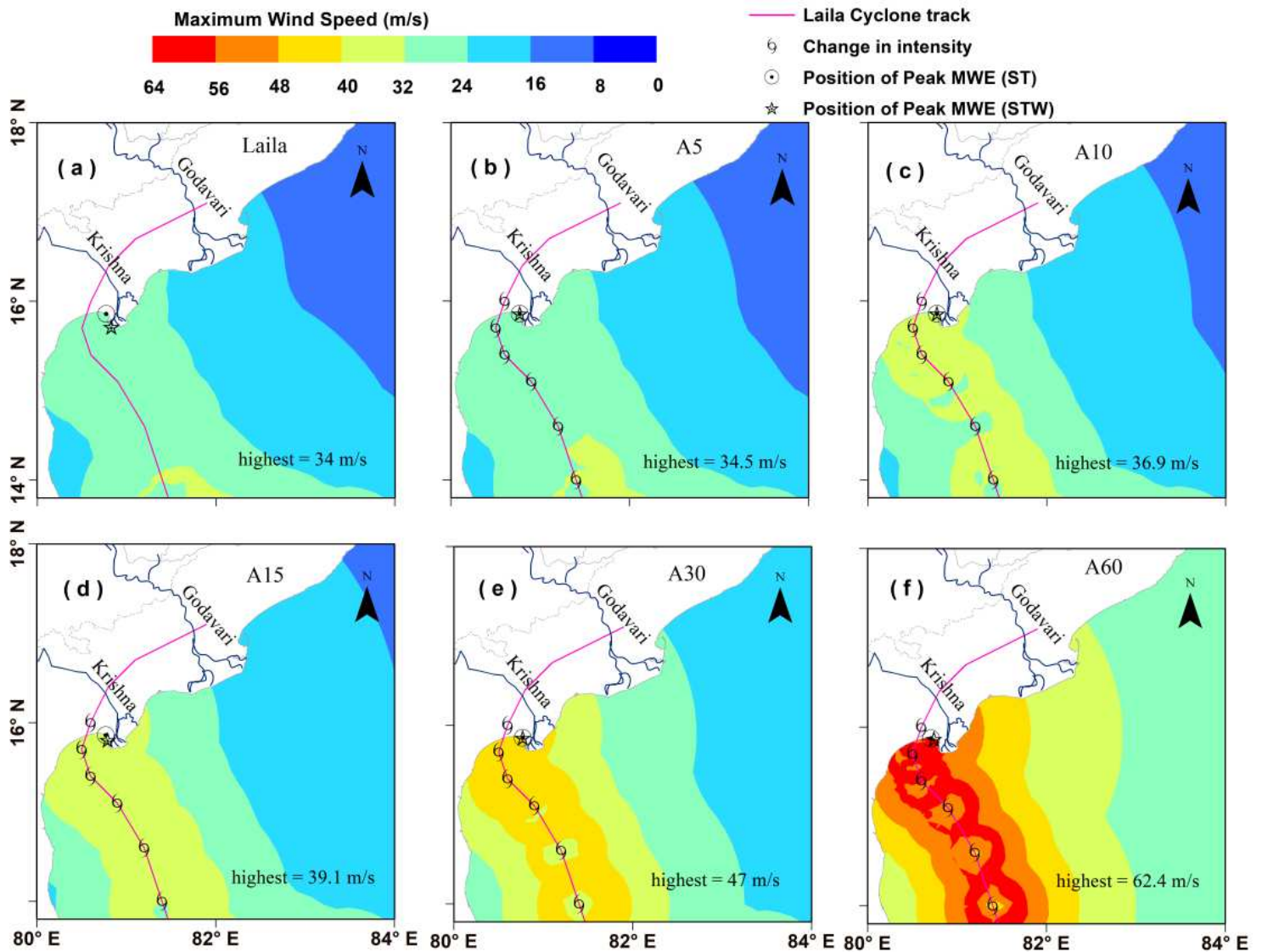


Figure 11

Comparison of observed and computed Water Levels at Visakhapatnam during an ESCS Hudhud 2014



**Figure 12**

Spatial plot of Maximum Wind Speed during (a) Laila Cyclone and for Test A Scenario where the wind speed increased by (b) 2.57 m/s (5 knots), (c) 5.14 m/s (10 knots), (d) 7.71 m/s (15 knots), (e) 15.4 m/s (30 knots), and (f) 30.86 m/s (60 knots) Note: The designations employed and the presentation of the material on this map do not imply the expression of any opinion whatsoever on the part of Research Square concerning the legal status of any country, territory, city or area or of its authorities, or concerning the delimitation of its frontiers or boundaries. This map has been provided by the authors.

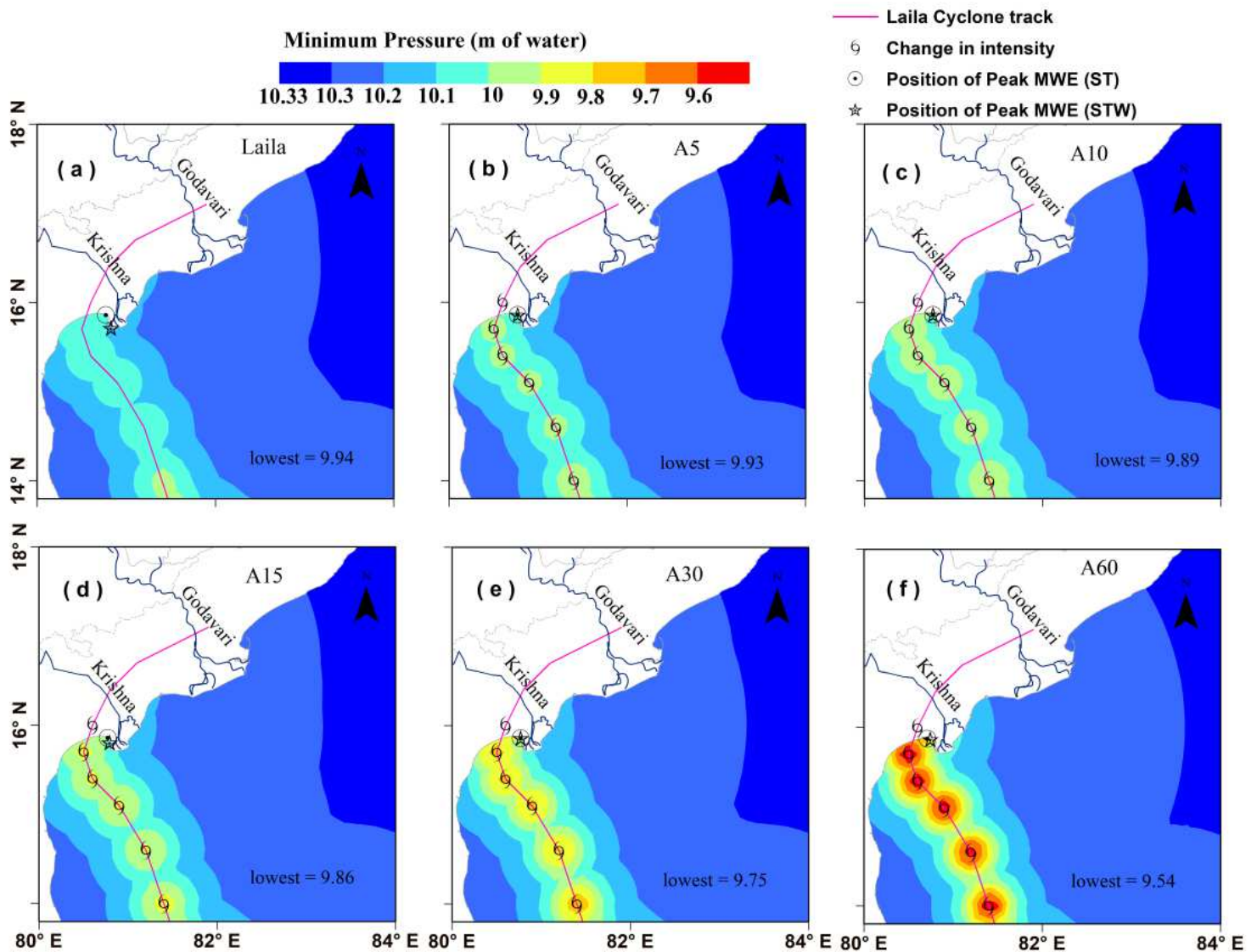


**Figure 13**

Spatial extent of Minimum Pressure during (a) Laila Cyclone, and for Test Scenario A where the wind speed increased by (b) 2.57 m/s (5 knots), (c) 5.14 m/s (10 knots), (d) 7.71 m/s (15 knots), (e) 15.4 m/s (30 knots), and (f) 30.86 m/s (60 knots) Note: The designations employed and the presentation of the material on this map do not imply the expression of any opinion whatsoever on the part of Research Square concerning the legal status of any country, territory, city or area or of its authorities, or concerning the delimitation of its frontiers or boundaries. This map has been provided by the authors.

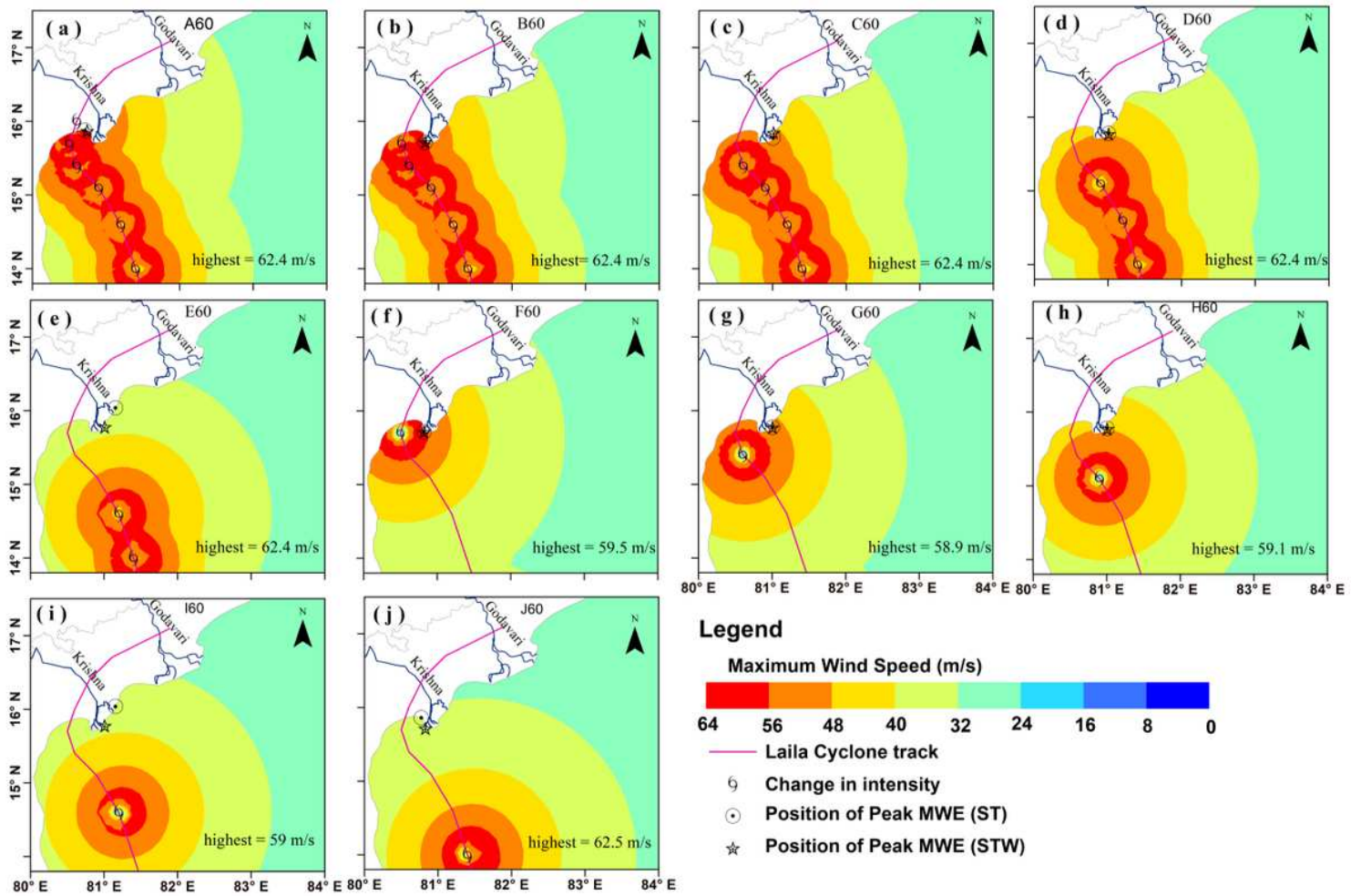


**Figure 14**

Spatial plot of Maximum Wind Speed with 30 m/s (60 knots) increase for different test scenarios (A - J)

Note: The designations employed and the presentation of the material on this map do not imply the expression of any opinion whatsoever on the part of Research Square concerning the legal status of any country, territory, city or area or of its authorities, or concerning the delimitation of its frontiers or boundaries. This map has been provided by the authors.

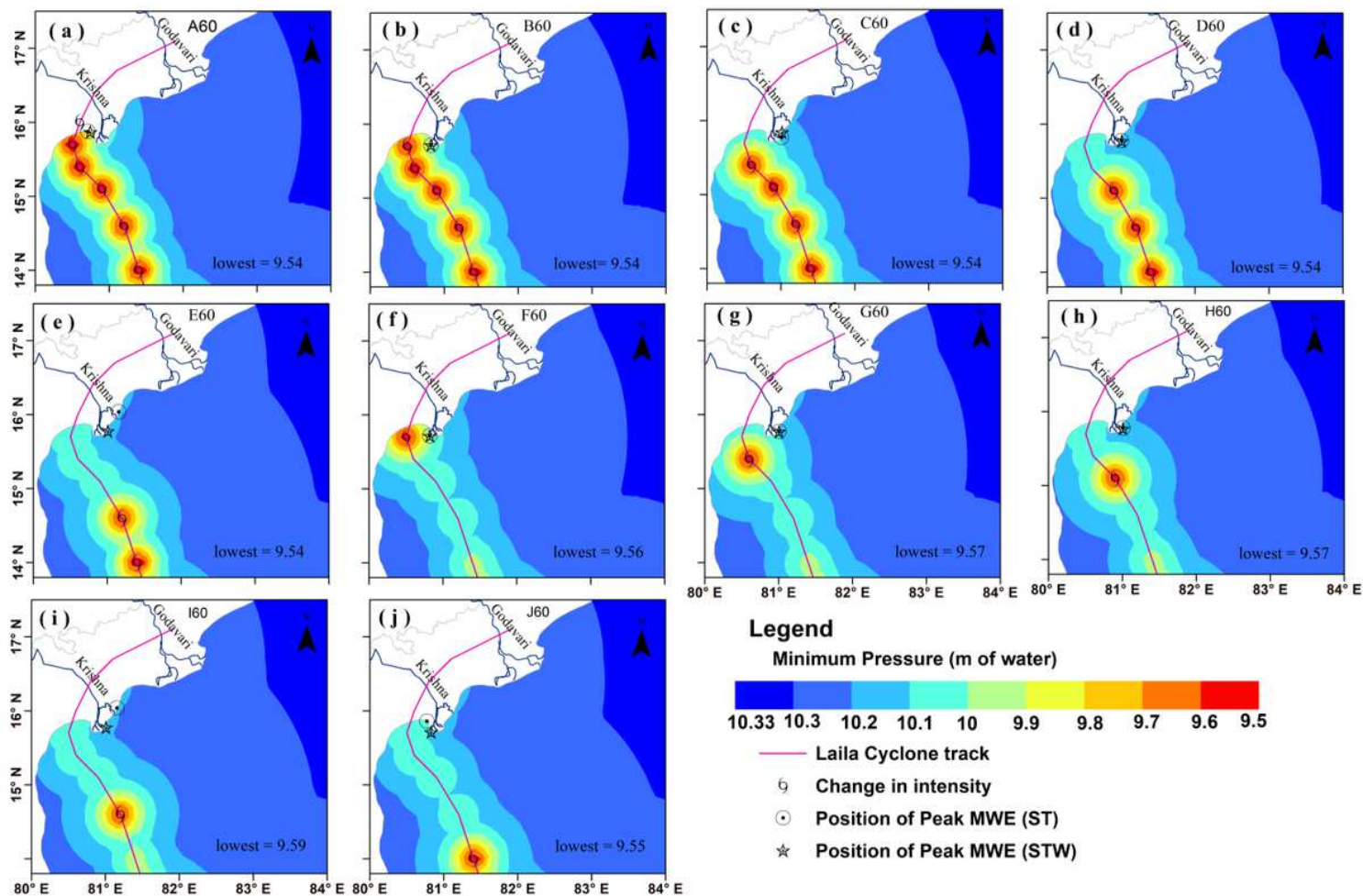


**Figure 15**

Spatial extent of Minimum Pressure for different Test Scenarios with an increasing wind speed by 30.86 m/s (60 knots) considered for the study Note: The designations employed and the presentation of the material on this map do not imply the expression of any opinion whatsoever on the part of Research Square concerning the legal status of any country, territory, city or area or of its authorities, or concerning the delimitation of its frontiers or boundaries. This map has been provided by the authors.

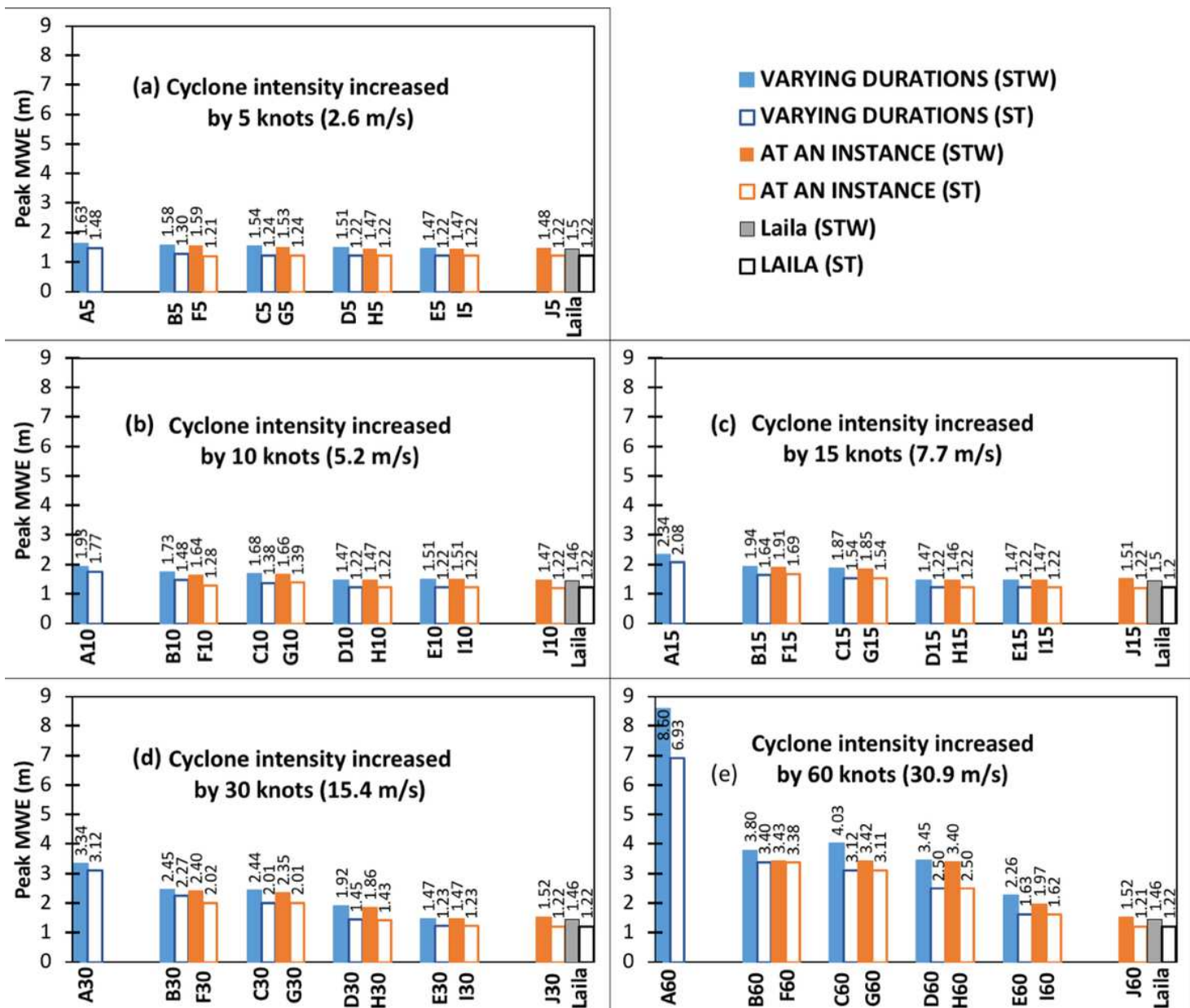


Figure 16

Peak Maximum Water Levels recorded by ST and STW along the K-G basin of Laila along with those of cyclone intensities increase by (a) (2.57 m/s (5 knots), (b) 5.14 m/s (10 knots), (c) 7.71 m/s (15 knots), (d) 15.4 m/s (30 knots), and (e) 30.86 m/s (60 knots) for 10 test scenarios

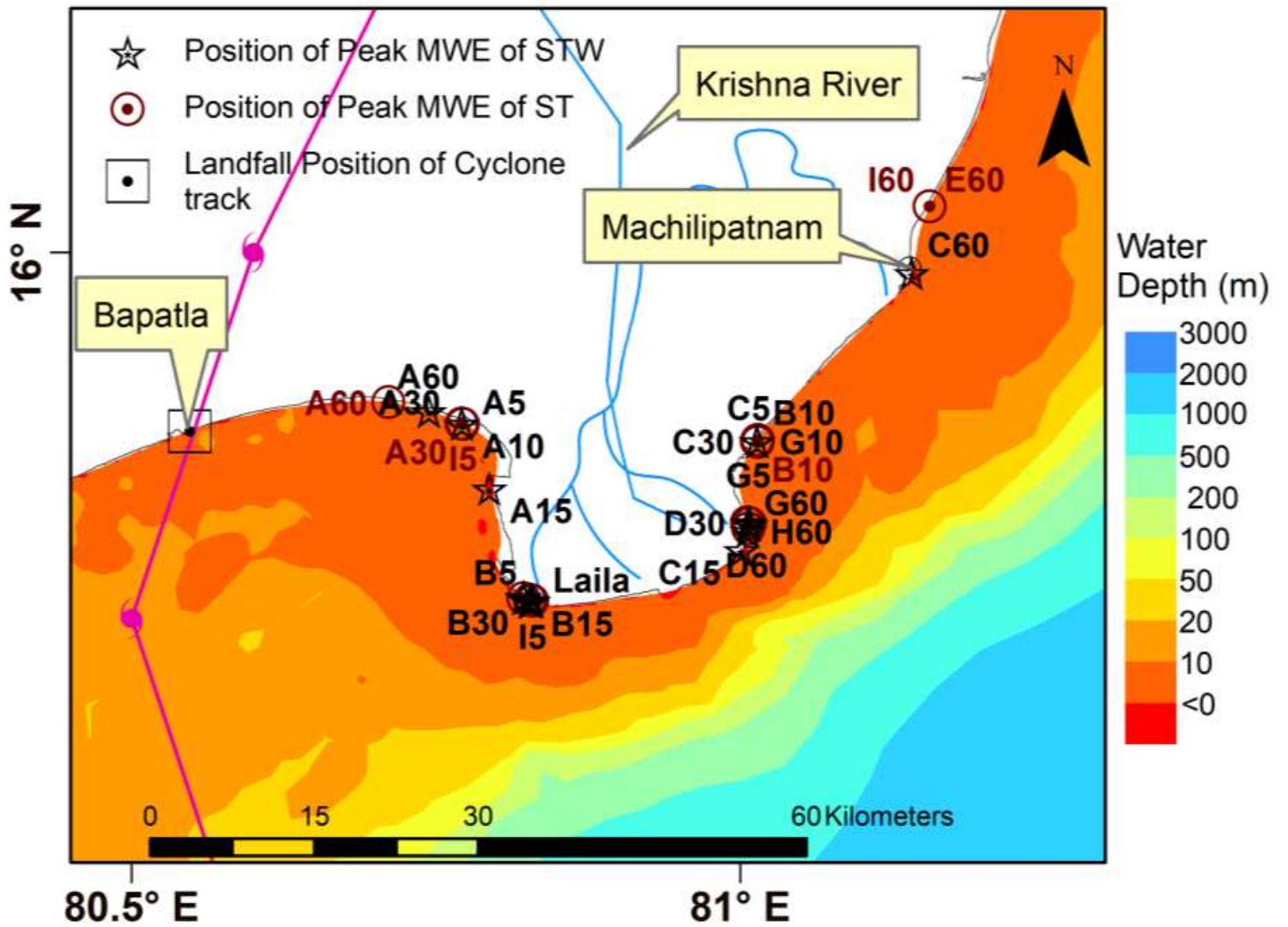
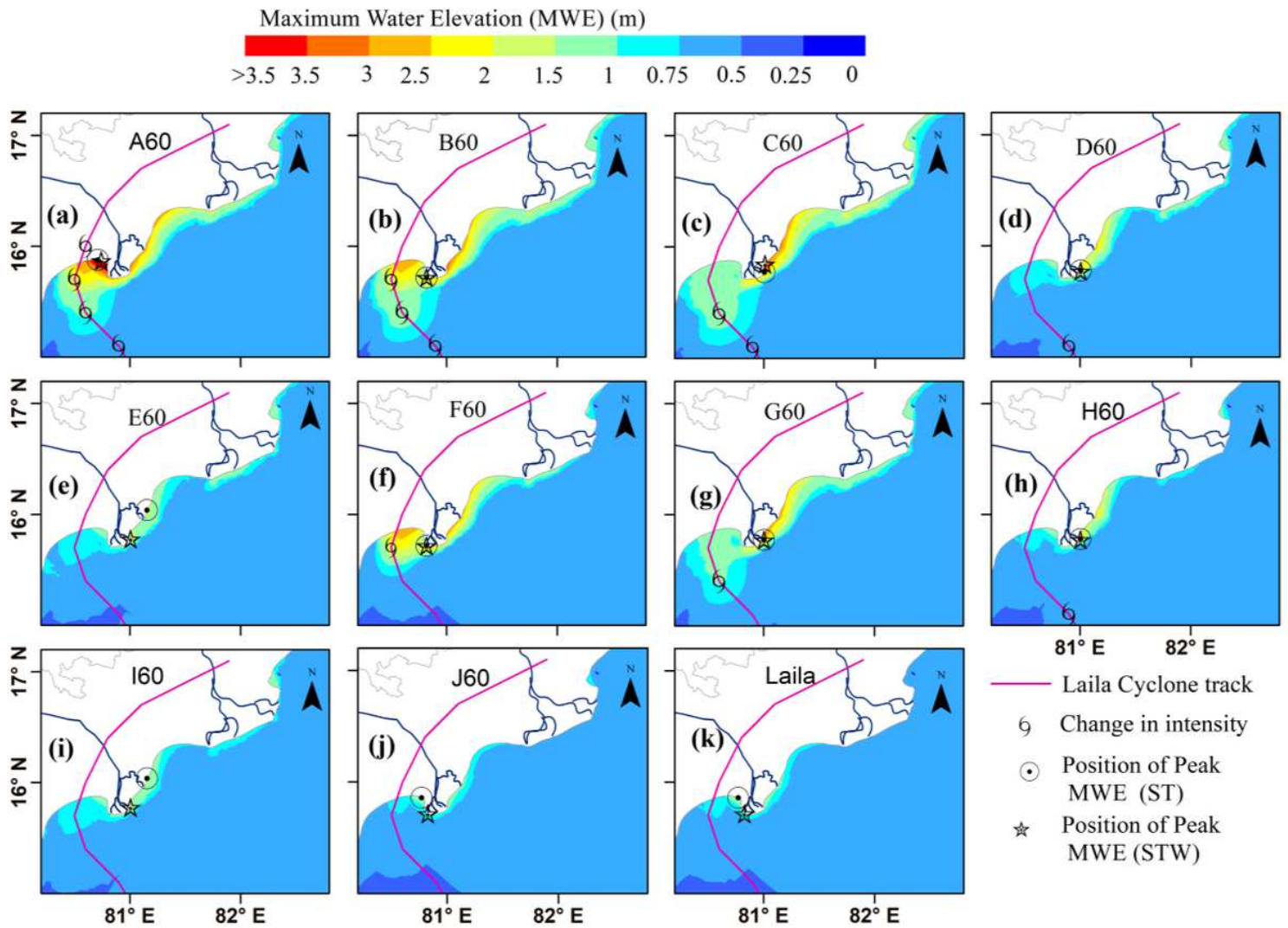


Figure 17

Location showing the Peak MWEs of STW and ST Note: The designations employed and the presentation of the material on this map do not imply the expression of any opinion whatsoever on the part of Research Square concerning the legal status of any country, territory, city or area or of its authorities, or concerning the delimitation of its frontiers or boundaries. This map has been provided by the authors.



**Figure 18**

Spatial plot showing MWE of STW along the K-G basin for cyclone with increasing wind speed by 30.86 m/s (60 knots) for different durations(a-j), and (k) Laila Note: The designations employed and the presentation of the material on this map do not imply the expression of any opinion whatsoever on the part of Research Square concerning the legal status of any country, territory, city or area or of its authorities, or concerning the delimitation of its frontiers or boundaries. This map has been provided by the authors.

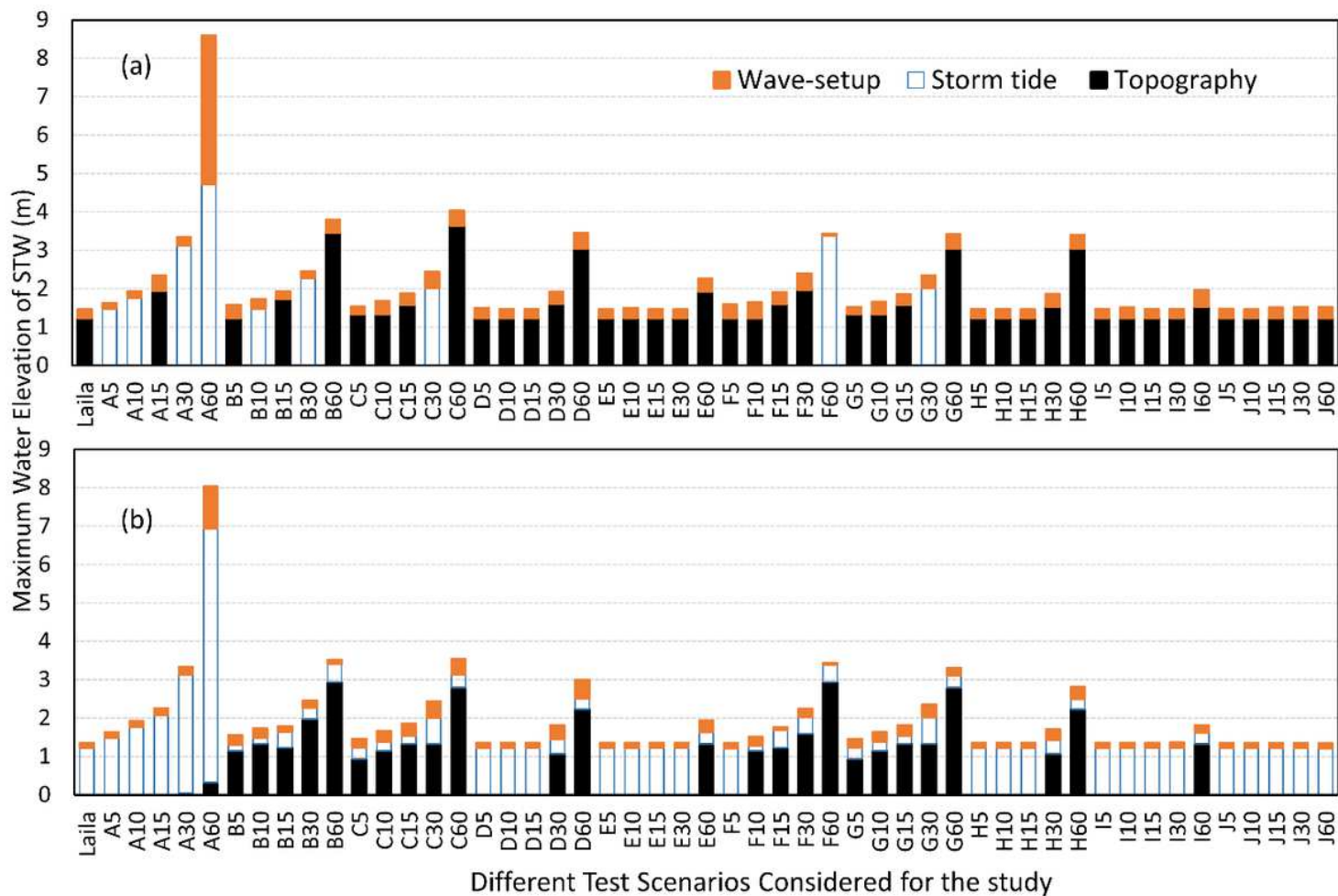


**Figure 19**

Wave contributions of all the numerical simulations at (a) location of peak MWE of STW (b) location of peak MWE of ST

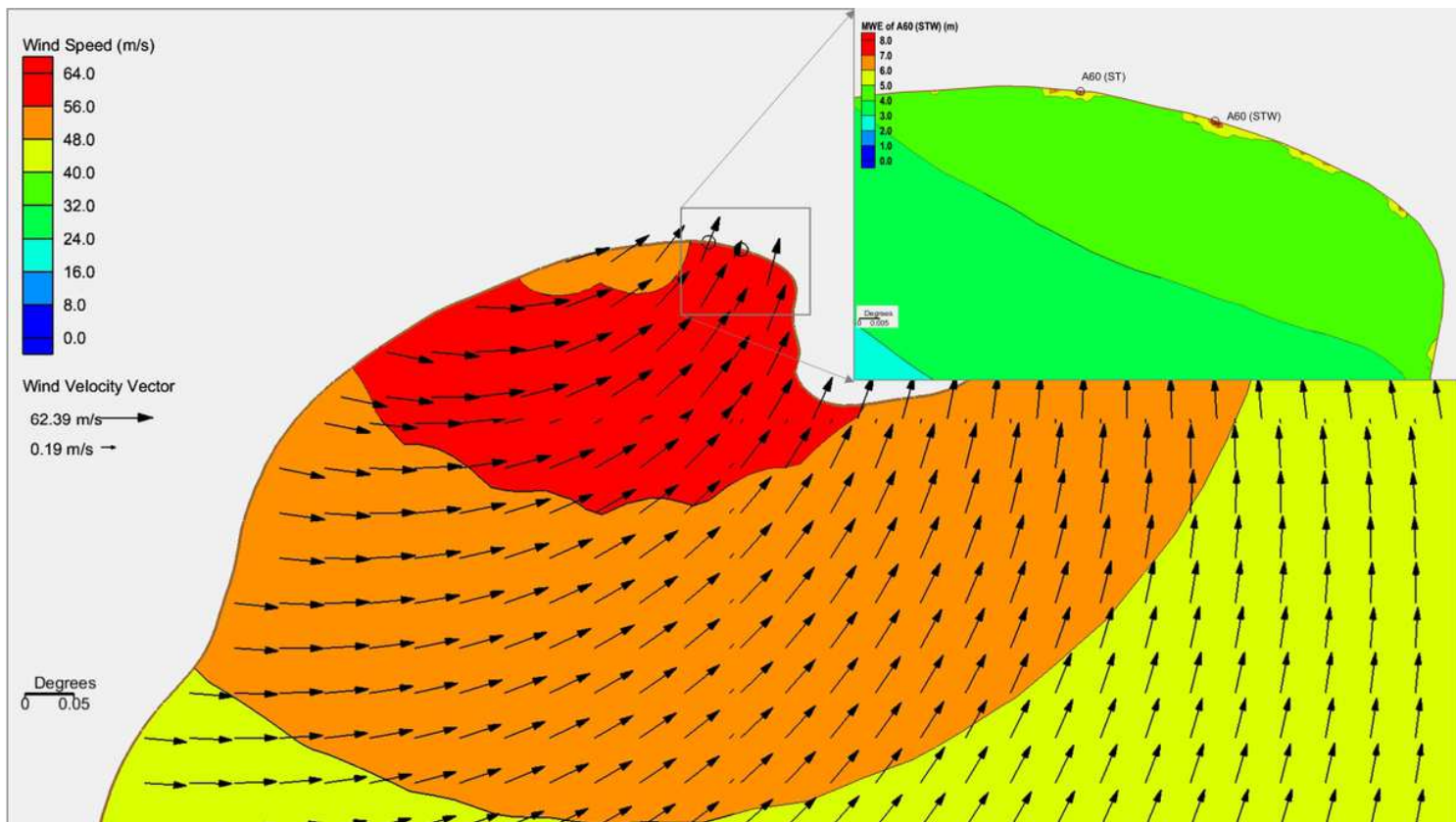


**Figure 20**

Wind field of Test A60 during the peak MWE for STW and the enlarged MWE showing the peak MWE (top right corner) Note: The designations employed and the presentation of the material on this map do not imply the expression of any opinion whatsoever on the part of Research Square concerning the legal status of any country, territory, city or area or of its authorities, or concerning the delimitation of its frontiers or boundaries. This map has been provided by the authors.

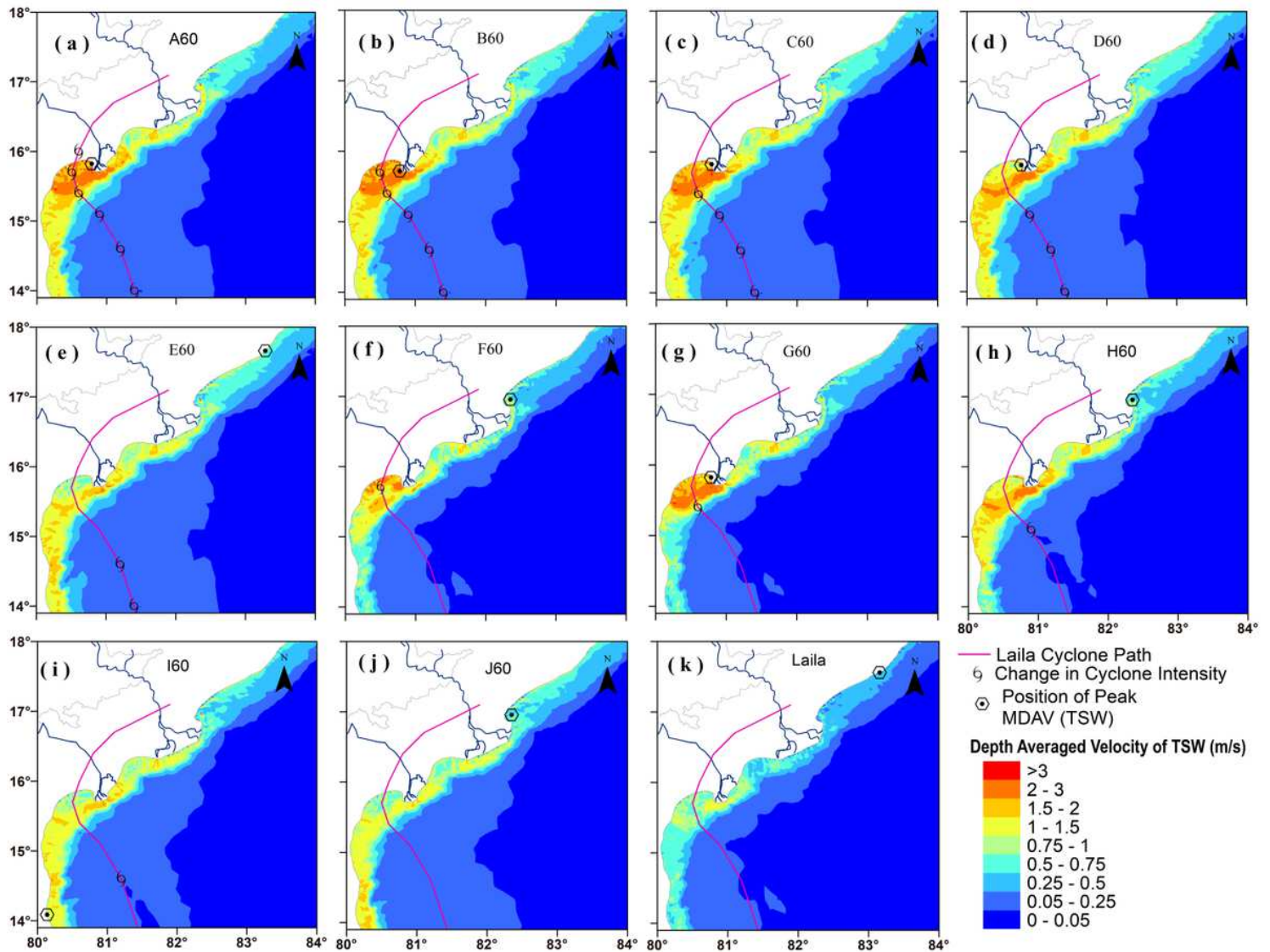


**Figure 21**

Spatial extent of Vavg\_max with increasing wind speed by 30.86 m/s (60 knots) for different durations considered for the study Note: The designations employed and the presentation of the material on this map do not imply the expression of any opinion whatsoever on the part of Research Square concerning the legal status of any country, territory, city or area or of its authorities, or concerning the delimitation of its frontiers or boundaries. This map has been provided by the authors.

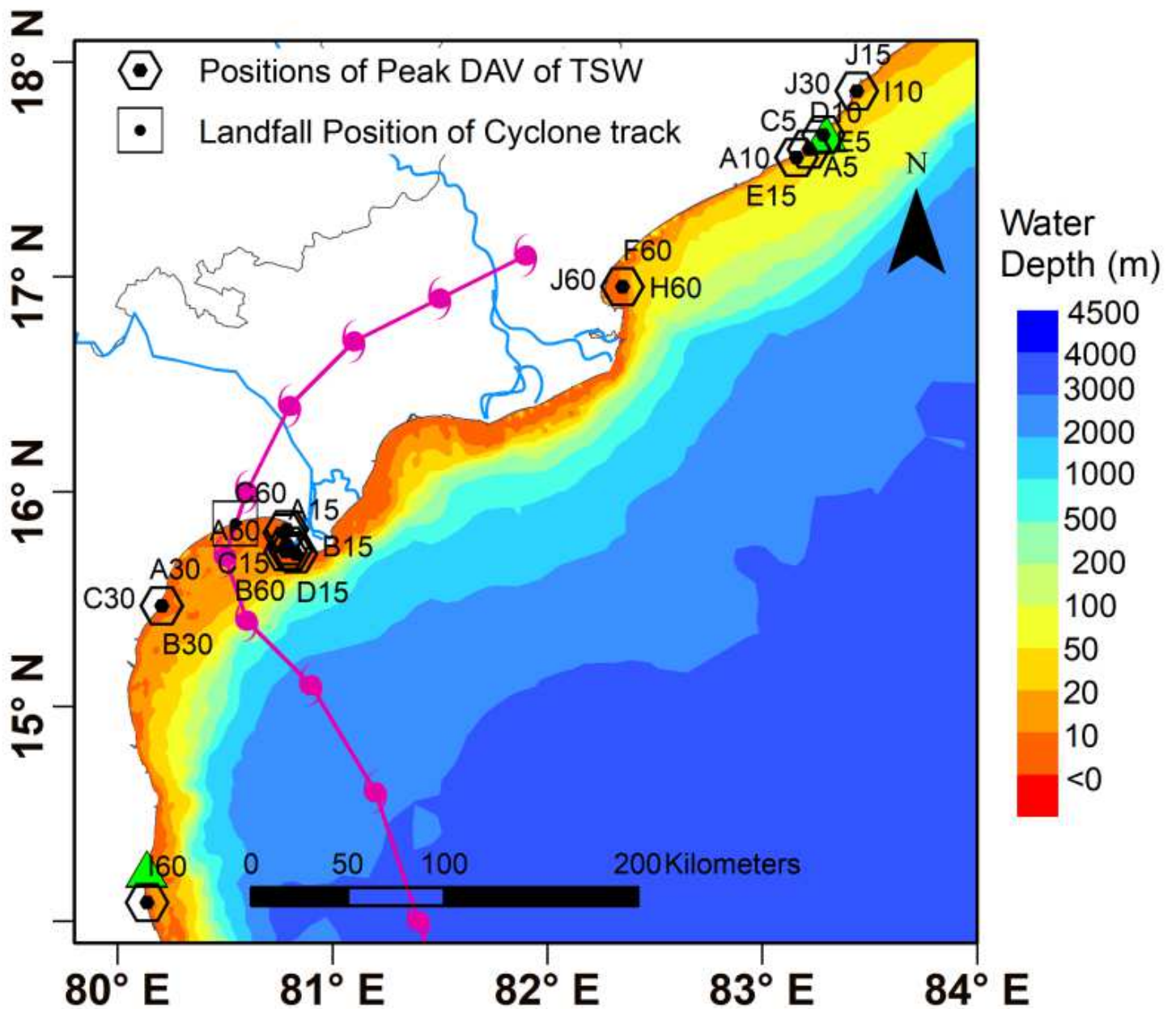


Figure 22

Locations of peak  $V_{avg\_max}$  for all the scenarios Note: The designations employed and the presentation of the material on this map do not imply the expression of any opinion whatsoever on the part of Research Square concerning the legal status of any country, territory, city or area or of its authorities, or concerning the delimitation of its frontiers or boundaries. This map has been provided by the authors.